Since January 2020 Elsevier has created a COVID-19 resource centre with free information in English and Mandarin on the novel coronavirus COVID-19. The COVID-19 resource centre is hosted on Elsevier Connect, the company's public news and information website.

European Journal of Medicinal Chemistry 244 (2022) 114853

Contents lists available at ScienceDirect

European Journal of Medicinal Chemistry

journal homepage: www.elsevier.com/locate/ejmech

Research paper

Easy access to α-ketoamides as SARS-CoV-2 and MERS M^{pro} inhibitors via the PADAM oxidation route

Sveva Pelliccia [a,*], Carmen Cerchia [a], Francesca Esposito [b], Rolando Cannalire [a], Angela Corona [b], Elisa Costanzi [c], Maria Kuzikov [d,e,f], Philip Gribbon [d,f], Andrea Zaliani [d,f], Margherita Brindisi [a], Paola Storici [c], Enzo Tramontano [b], Vincenzo Summa [a,**]

[a] Department of Pharmacy, University of Naples Federico II, via D. Montesano 49, 80131, Naples, Italy
[b] Dipartimento di Scienze della Vita e dell'Ambiente, Cittadella Universitaria di Monserrato, Cagliari, Monserrato, SS-554, Italy
[c] Protein Facility, Elettra - Sincrotrone Trieste S.C.p.A., SS 14 - km 163, 5 in AREA Science Park, Trieste, Basovizza, 34149, Italy
[d] Fraunhofer Institute for Translational Medicine and Pharmacology (ITMP), Schnackenburgallee 114, Hamburg, 22525, Germany
[e] Department of Life Sciences and Chemistry, Jacobs University Bremen, 28759, Bremen, Germany
[f] Fraunhofer Cluster of Excellence for Immune-Mediated Diseases CIMD, Theodor-Stern-Kai 7, 60596, Frankfurt am Main, Germany

ARTICLE INFO

Keywords:
SARS-CoV-2
Main protease inhibitors
α-ketoamides
PADAM-Oxidation
Multicomponent reactions

ABSTRACT

SARS-CoV-2 caused worldwide the current outbreak called COVID-19. Despite multiple countermeasures implemented, there is an urgent global need for new potent and efficient antiviral drugs against this pathogen. In this context, the main protease (M^{pro}) of SARS-CoV-2 is an essential viral enzyme and plays a pivotal role in viral replication and transcription. Its specific cleavage of polypeptides after a glutamine residue has been considered as a key element to design novel antiviral drugs. Herein, we reported the design, synthesis and structure-activity relationships of novel α-ketoamides as covalent reversible inhibitors of M^{pro}, exploiting the PADAM oxidation route. The reported compounds showed μM to nM activities in enzymatic and in the antiviral cell-based assays against SARS-CoV-2 M^{pro}.

In order to assess inhibitors' binding mode, two co-crystal structures of SARS-CoV-2 M^{pro} in complex with our inhibitors were solved, which confirmed the covalent binding of the keto amide moiety to the catalytic Cys145 residue of M^{pro}. Finally, in order to interrogate potential broad-spectrum properties, we assessed a selection of compounds against MERS M^{pro} where they showed nM inhibitory potency, thus highlighting their potential as broad-spectrum coronavirus inhibitors.

1. Introduction

At the end of 2019, a serious outbreak of putative pneumonia was firstly observed in Chinese Wuhan city leading to the discovery of a novel virus, shortly after named Severe Acute Respiratory Syndrome Coronavirus-2 (SARS-CoV-2), due to its high genetic (79%) similarity with SARS-CoV-1. The newly identified virus rapidly spread worldwide and, in March 2020, the World Health Organization (WHO) declared the SARS-CoV-2 infection and the associated serious coronavirus disease 2019 (COVID-19) as a global pandemic, affecting both the healthcare system and the global economy, with almost more than six million of deaths [1,2]. The scientific community reacted immediately to characterize both the viral genome and potential viral and host key therapeutic targets, mostly taking advantage of the acquired knowledge from previous human pathogenic CoVs, such as SARS-CoV and MERS-CoV [3–5]. Till the half of 2021, the most effective procedures to slow down viral spread have been the social distancing and the use of respiratory protective devices. However, the unprecedented rapidity in developing effective vaccines contributed to effectively hold off the viral spread at least in industrialized countries. However, the development of novel antiviral drugs still represents a priority for human health for different reasons, such as early efficacious treatment for the new infections, prevention for the people that have had close contact with positive subjects, treat people who cannot be vaccinated (e.g., immunocompromised persons, people living in developing countries) and in the case of availability of pan CoVs inhibitors prevent new spillover infection and

* Corresponding author.
** Corresponding author.
E-mail addresses: sveva.pelliccia@unina.it (S. Pelliccia), vincenzo.summa@unina.it (V. Summa).

https://doi.org/10.1016/j.ejmech.2022.114853
Received 29 July 2022; Received in revised form 11 October 2022; Accepted 11 October 2022
Available online 17 October 2022

mitigate the new variants that could overcome vaccines.

SARS-CoV-2 is an enveloped virus containing a ~30-kb encapsidated (ss- (+))-RNA belonging to β-CoV sub-family. The genomic RNA encodes for two large overlapping polyprotein precursors (pp1a and pp1ab), four structural proteins (spike, envelope, membrane, and nucleocapsid), and several accessory proteins (1, 2, 6). Pp1a and pp1b cleavage into individual nonstructural proteins is essential for viral genome replication and is carried out by two viral proteases: the main protease (M^{pro}, also named 3CL protease) and the papain-like protease [6,7]. Notably, M^{pro} is responsible for the release of most of the nonstructural proteins and shows a high degree of homology across human CoVs [8]. As demonstrated also for SARS-CoV-1, in its active form, M^{pro} is a dimer with each monomer containing the substrate binding site located in a wide cleft, hosting the Cys145-His41 catalytic dyad [9,10]. The most specific recurrent P2–P1–P1' sequence is Leu-Gln-Ser (or Ala and Gly instead of Ser in P1'). Furthermore, this cleavage sequence is not known in any human protease, allowing the identification of novel selective drugs [11–13]. Based on the knowledge of the catalytic site of M^{pro} and the substrate binding specificity, a favorable approach is the design of covalent reversible inhibitors that are recognized as an important component in drug discovery and therapeutics for their safety and potency against different targets, and for their fast development as reported for HCV first generation inhibitors. This strategy has indeed afforded Boceprevir and Telaprevir, two peptidomimetic α-ketoamides serine protease inhibitors approved for HCV genotype 1 infected patients, and much more importantly resulted a very effective strategy also against SARS-CoV-2 with the recent approval of Nirmaltrelvir [14]. In aid, a large number of crystal structures is available for the M^{pro} of SARS-CoV-2 and of other human CoVs as apoenzymes and especially in complex with peptidomimetic covalent reversible inhibitors.

The specific SARS-CoV-2 M^{pro} inhibitors reported so far possess as Gln mimetic a 5-membered ring derivative (γ-lactam) in P1 that enhanced the inhibition up to 10- fold. Despite lacking this requirement also the co-crystal structures of SARS-CoV-2 M^{pro} in complex with Boceprevir (PDB: 7COM) and Telaprevir (PDB:7C7P) [15,16], have been solved resulting as SARS-CoV-2 M^{pro} inhibitors. Taking into account the cocrystal structures of SARS-COV-2 M^{pro} in complex with Boceprevir and Telaprevir, very recently by a hybridization strategy a series of dipeptides has been reported (MI23 and MI30) [17] (Fig. 1). The glutamine γ-lactam analog11 has been fixed in P1, as well as the P2 bicyclo proline moiety derived from either Boceprevir or Telaprevir that suitably occupied the S2 pocket of SARS-COV-2 M^{pro}; variability has been only explored in the P3 region, through the insertion of different hydrophobic subgroups able to establish interactions with the S4 pocket. The small, less bulky and electrophilic aldehyde has been chosen as warhead. Two and half years of global drug discovery efforts have delivered two reversible covalent inhibitors so far, namely the IV prodrug PF-07304814 [18] and the recently approved orally available Nirmatrelvir (PF-07321332) [14] (Fig. 1).

Taking into account these structural requirements, we report herein a series of dipeptides exploring the P1' region through the use of α-ketoamide moiety as "warhead" which, unlike the aldehyde, offers the possibility to be derivatized using different alkyl/aryl groups. Moreover, the α-ketoamide motif has been considered for its extensive use as a privileged motif in drug discovery and it has already been successfully embedded in the structure of potent M^{pro} inhibitors [19,20]. Furthermore, preserving the γ-lactam in P1 we used a residue of proline in P2 which conferred a β-turn conformation of peptidomimetic structure, with restricted *N*-Cα conformation, that pointed this residue into the S2 pocket. Additionally, benzyloxycarbonyl (Cbz) and 2,4 dichlorophenoxy acetyl groups have been chosen as lipophilic *N*-capping groups, for their better ability to occupy the S4 pocket [16]. In order to identify a procedure to obtain as fast as possible the new potential protease inhibitors, we decided to exploit an easy combinatorial access to peptidomimetic compounds, through the involvement of the milestone three-component Passerini reaction followed by Amine Deprotection and Acyl Migration (PADAM) [21,22]. When enantiomerically pure starting materials (I and II) were employed, the PADAM reaction generated a new chiral center (IV), with the formation of two diastereoisomers but considering the final desired α-oxoamides products (VII), diastereoselection at this level is unimportant. Therefore, this efficient synthetic route provided a set of α-ketoamide derivatives (VII) in a reduced time through the final

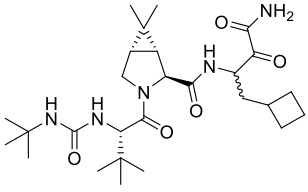

Boceprevir
IC_{50} SARS-CoV-2 : 4.13 μM

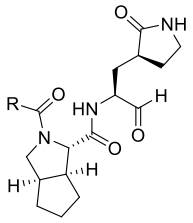

MI23: R= 3,5 difluorophenethyl
IC_{50} SARS-CoV-2 : 7.6 nM

MI30: R= 2,4 dichlorophenoxyacetyl
IC_{50} SARS-CoV-2 : 17.2 nM

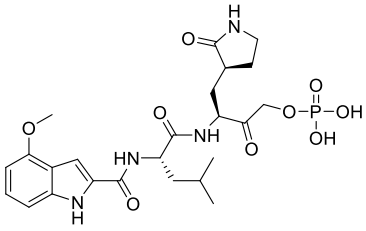

Lufotrelvir (PF-07304814)
Ki SARS-CoV-2 : 174 nM

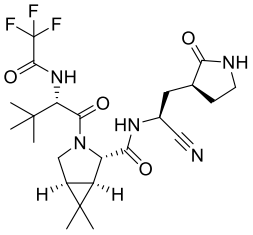

Nirmatrelvir (PF-07321332)
Ki SARS-CoV-2 : 3.11 nM

Fig. 1. SARS-CoV-2 M^{pro} inhibitors previously reported.

oxidation route of α-hydroxy-β-amino amides (VI) (Fig. 2 A).

2. Results and discussion

2.1. Chemistry

From a synthetic point of view, over the past decades a vast variety of procedures for the preparation of α-ketoamides have been developed, following a C(2)-oxidation of 2-hydroxyamides or 2-aminoamides or considering methodologies centered on C(1)–C(2) σ-bond formation and C(2)−R/Ar bond forming processes. Also, the palladium-catalyzed double-carbonylative amination reactions have been reported [23,24].

The synthetic procedure for α-ketoamides peptidomimetic M^{pro} inhibitors previously reported, has provided the synthesis of both *N*-deprotected γ-lactam methyl ester and *N*-capped dipeptides and after their subsequent coupling, followed by ester reduction into the corresponding alcohol and oxidation into the aldehyde. The nucleophilic addition of isocyanides in acetic acid, generated the α-acetoxy amides converted into α-hydroxy amides through removal of acetyl group. Finally, the oxidation of alcohols using Dess Martin periodinane generated the desired α-ketoamides [20].

The isocyanide based multicomponent reaction approach, firstly reported by Banfi et al., used an easy and fast PADAM oxidation route, starting from a Passerini reaction in aprotic solvent, followed by amine deprotection and intramolecular acyl migration, forming the α-hydroxy-β-amino amide derivatives, subsequently used for the synthesis of attractive α-oxo-β-amino acids [21,22] (Fig. 1). The starting γ-lactam aldehyde (**3**) was separately synthesized through reduction of the commercially available γ-lactam ester (**1**) into alcohol (**2**) with lithium borohydride in tetrahydrofuran for 2 h and oxidation into aldehyde **3** using Dess Martin periodinane in dichloromethane for 1 h (Scheme 1).

The obtained aldehyde **3** was used for further Passerini reactions combined with different *N*-derivatized prolines carboxylic acids **4a-c** and various isocyanides **5a-f** (commercially available or synthesized) (Scheme 2). The product obtained by Passerini reaction were purified by silica gel chromatography with yields ranging from 61% to 85%. Although Passerini reaction led to the α-hydroxy ketone derivatives **6a-j** in approximately 2:1 diastereomeric ratio as determined by ^{1}H NMR. The treatment with trifluoroacetic acid for Boc removal, followed by *in situ* transacylation involving brief treatment with triethylamine in dichloromethane overnight, provided α-hydroxy-β amino acids **8a-j**, easily converted into our target α-oxo-β-amino acids **9 a-j** using Dess Martin periodinane in dichloromethane for 1 h (Table 1).

It's worth of note that thanks to this versatile, fast and easy synthetic route, several parallel preparations of α-hydroxy-β amino acids can be run and processed in two days, without purification of Boc deprotected and transacylated products (to validate the method, the synthesis of the first product was monitored step by step via ^{1}H NMR and/or Mass spectra).

We synthesized 10 different α-ketoamides with a constrained amino acid as proline in P2 derivatized with hydrophobic groups in P3.

2.2. Broad-spectrum effect against SARS-CoV-2 M^{pro} and MERS-CoV M^{pro}

The synthesized compounds were screened at 20 μM concentration on SARS-CoV-2 M^{pro}, using GC376 as reference inhibitor [25] (Table 2). Detected activities were normalized to the inhibitory activity of GC376 that was used as positive control and set to 100% (positive control) and to values measured for the DMSO control, set to 0% inhibition (negative control). The compounds were tested without or in the presence of a reducing agent, such as TCEP (5 mM) in order to evaluate its effect on compound inhibitory activity [18]. The sensitivity to TCEP is likely due to its effects on compound reactivity toward the Cys-145 moiety in the SARS-CoV-2 M^{pro} catalytic domain. Multiple enzymatic studies on M^{pro} have used TCEP to reduce protein oxidation and maintain consistency with those protocols.

Regardless of the presence of TCEP, all the compounds were able to

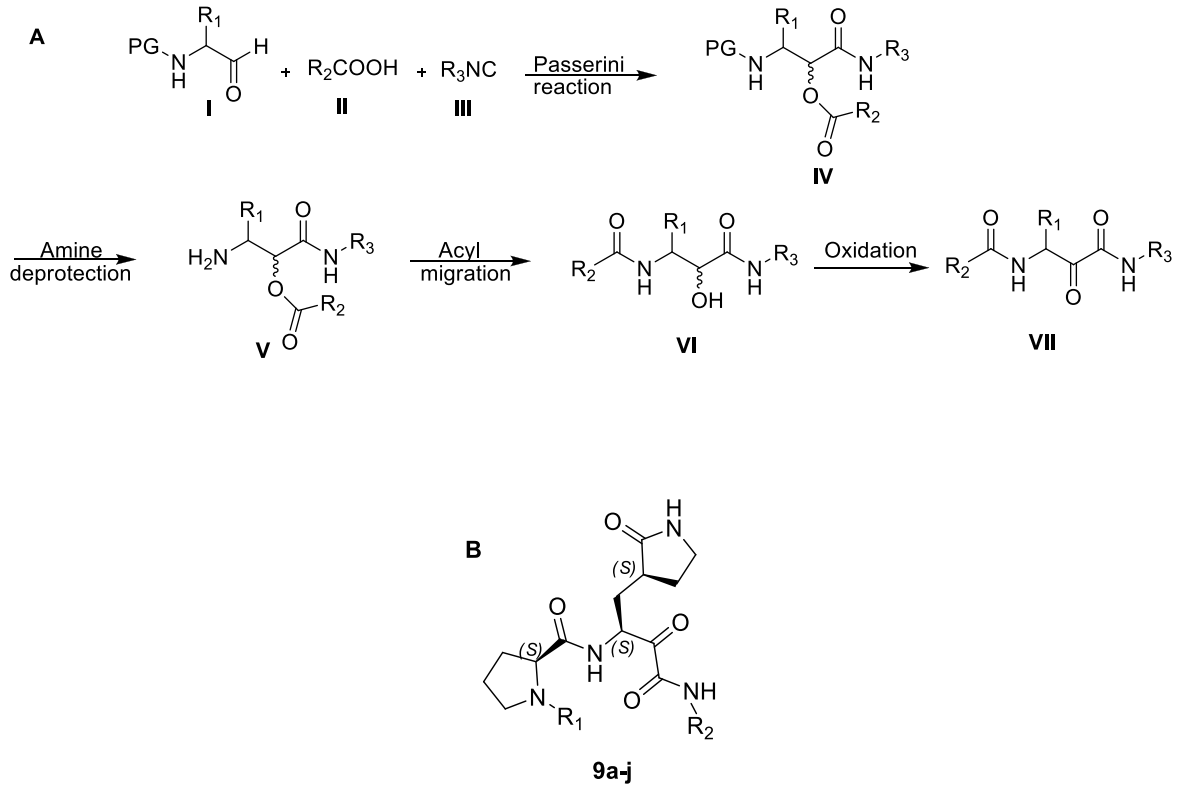

Fig. 2. A. PADAM strategy for the α-hydroxy-β-amino amides. **B**. General structure of our synthesized α-ketoamides (**9a-j**).

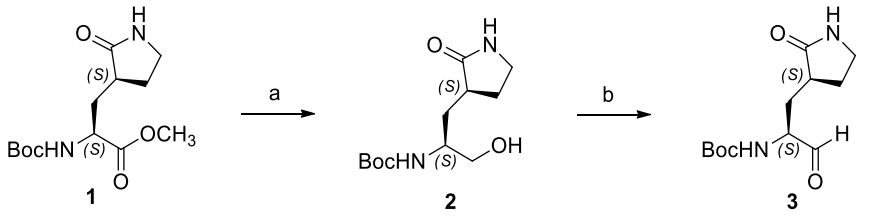

[a]Reagents and conditions: (a) Lithium borohydride, tetrahydrofuran, 0°C to rt, 2h, yield 53%; (b) Dess Martin Periodinane, dichloromethane, 2h, yield 91%

Scheme 1. Synthesis of γ-lactam aldehyde (3).

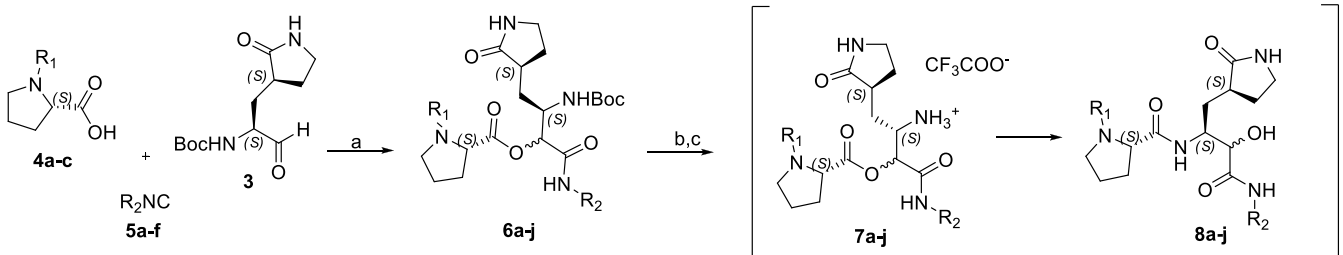

R_1= Benzyloxycarbonyl(Cbz); 2,4 dichlorophenoxy acetyl; 1-benzyl sulfonyl
R_2= Benzyl, Phenethyl, 2,4-dimethoxy benzyl, 3-trifluoromethyl benzyl, 2-fluoro phenethyl, 2-methoxy phenethyl

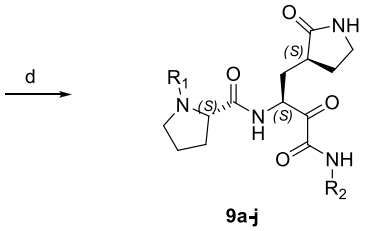

[a]Reagents and conditions: (a) Dichloromethane, rt, overnight, yield:50-60%,dr:70/30; (b) Dichloromethane/trifluroacetic acid 3:1, rt, 1h, quantitative;(c)Dichloromethane/triethylamine 3:1, rt, overnight, quantitative; (d)Dess Martin Periodinane, Dichloromethane, rt, 2h, yield:19-76%

Scheme 2. Synthesis of α-ketoamides (**9a-j)** via PADAM oxidation route.

Table 1
Synthesized α-ketoamides.

Compound	R_1	R_2
9a	Cbz	Phenethyl
9b	Cbz	2-Fluoro Phenethyl
9c	Cbz	2-Methoxy Phenethyl
9d	2,4 dichlorophenoxy acetyl	Benzyl
9e	2,4 dichlorophenoxy acetyl	Phenethyl
9f	2,4 dichlorophenoxy acetyl	2,4- Dimethoxy Phenethyl
9g	1-benzyl sulfonyl	Benzyl
9h	2,4 dichlorophenoxy acetyl	2-Trifluoromethyl Phenethyl
9i	2,4 dichlorophenoxy acetyl	2-Fluoro Phenethyl
9j	2,4 dichlorophenoxy acetyl	2-Methoxy Phenethyl

inhibit the M^{pro} with different potencies in the micromolar/submicromolar/nanomolar range; four compounds **9a**, **9e**, **9f**, **9g** displayed an inhibition of the protease yielding IC_{50} values below 3 μM, while three compounds these**9b**, **9c**, **9d**, showed M^{pro} inhibition values in submicromolar range. Two compounds **9i** and **9j** resulted very potent, showing IC_{50} values on M^{pro} of 26 nM and 30 nM, respectively. These results suggested a role of the ketoamide substituent rather than the *N*-proline capping group; indeed, six (**9a**, **9b**, **9c**, **9e**, **9i**, **9j**) out of the nine most potent inhibitors possess a phenethyl (**9a**, **9e**), or a *o*-fluoro phenethyl (**9b**, **9i**) or a *o*-methoxyphenethyl (**9c**, **9j**) at the ketoamide nitrogen while each pair of derivatives differs only for the presence of the Cbz and the 2,4 dichlorophenoxy acetyl groups as lipophilic pendants.

On the other hand, compounds **9d** and **9g**, having a shorter benzyl ketoamide, constituted an exception with respect to the above finding. These compounds reported IC_{50} values of 1.71 (**9g**) and 0.21 (**9d**) μM, showing that the combination of *N*-capping groups and ketoamide substituent could be relevant in some case for the enzyme inhibition. On the contrary, substitution of the benzyl ketoamide with a *o*-trifluoromethyl group, gave an inactive compound (**9h**), with $IC_{50} > 30$ μM.

Interestingly, compounds **9i** and **9j** that present a dichlorophenoxy acetyl *N*-capping group and *o*-fluoro phenethyl (**9i**) or *o*-methoxyphenethyl (**9j**) ketoamide showed IC_{50} of 26 and 30 nM against M^{pro}, highlighting the possibility to insert both electron withdrawing and electron donating groups on the phenyl ring of ketoamide moiety without compromising the activity.

Due to the promising M^{pro} inhibition and antiviral activity of these analogs (see next paragraph) against SARS-CoV-2, we investigated the inhibitory activities of our compounds on the main protease of the human-pathogenic MERS-CoV as well.

Table 2
Structures and activities of α-ketoamides as SARS-CoV-2 and MERS-CoV M^{pro} inhibitors.

cmp	M^{pro} SARS-COV-2 IC_{50} μM [a]	M^{pro} MERS IC_{50} μM [a]	EC_{50} μM [b]	EC_{50} μM + CP100356 (2 μM) [b]	CC_{50} μM + CP100356 (2 μM) [c]	SI + CP100356 (2μM)
9a	1.66 ± 0.02	20.25 ± 1.42	15.7 ± 8.3	14.8 ± 6.1	>100 (100%)[e]	>6.7
9b	0.144 ± 0.02	>30 (77%)[d]	>100	22.7 ± 3.1	>100	>4.4
9c	0.10 ± 0.002	0.06 ± 0.002	>100	30.3 ± 3.3	>100	>3.3
9d	0.21 ± 0.02	0.07 ± 0.0036	>100 >100	4.5 ± 1.31	>100 (100%)[e]	>22.2
9e	2.63 ± 0.11	20.01 ± 1.59	>100	8.03 ± 1.36	>100 (100%)[e]	>12.5
9f	1.93 ± 0.16	>30 (59%)[d]	>100 >100	7.13 ± 1.02	>100	>14
9g	1.71 ± 0.14	>30 (67%)[d]	>100	44 ± 24	>100	>2.3
9h	>30 (57%)[d]	>30 (73%)[d]	>100	>100	>100	>100
9i	0.026 ± 0.002	20.3 ± 5.08	>100	18.74 ± 2.9	>100	>100
9j	0.03 ± 0.003	24.6 ± 2.9	>100	9.61 ± 0.31	>100	>10.4
GC376	0.0005 ± 0.00003	0.0007 ± 0.00003	4.32 ± 1.33	0.76 ± 0.27	>100	>131

[a] IC_{50} values represent the average of two independent experiments which were determined based on at least 10 compound concentrations in triplicate. Errors are given by the ratio between the standard deviation and the square root of the number of measurements.

[b] EC_{50} values of M^{pro} inhibitors in Vero E6 cells calculated with Prism 9. Version 9.1.2 via non-linear regression. Vero E6-GFP were maintained in Dulbecco's modified Eagle's medium (DMEM; Gibco) supplemented with 10% v/v fetal bovine serum (FBS; Gibco), 0.075% Sodium Bicarbonate (7.5% solution, Gibco) and 1x Pen-strep (Euroclone) and kept under 5% CO_2 on 37 °C. Cells were incubated with the control compounds at different concentrations and the virus at MOI 0.01. GC376 compound was used as positive control, in presence of 2 μM P-gp inhibitor CP-100356. Means ± SDs from two biological experiments in triplicates are presented.

[c] CC_{50} values of M^{pro} inhibitors in Vero E6-GFP cells calculated as a percentage of fluorescence of untreated controls, minus blancs (empty wells) with Prism 9. Version 9.1.2 (225) via non-linear regression. Cells were incubated with different concentrations of the inhibitor in presence of 2 μM P-gp inhibitor CP-100356. The experiments represent average and standard deviation of at least two independent experiments in triplicate.

[d] % of inhibition of the M^{pro} at 30 μM.

[e] Residual cell viability at the highest concentration tested.

Compounds **9c** and **9d** were discovered to be two of the most effective representatives of MERS-CoV M^{pro} inhibitors with IC_{50} values of 60 and 70 nM, respectively.

The reported α-ketoamides represent a novel class of broad-spectrum inhibitors that target M^{pro} of SARS-CoV-2, and MERS-CoV, with a comparable (**9c**) or highest (**9d**) potency against MERS-CoV M^{pro} and SARS-CoV-2.

Combining the activity data with results obtained through docking studies and X-ray structures (see next Paragraphs), a preliminary SAR analysis could be rationalized. The presence of 2-fluoro (**9b**) or 2-methoxy (**9c**) substituents on P1′ phenethyl group allows establishing additional hydrophobic interactions with Thr26 and Thr25 of the S1' pocket of SARS-CoV-2 M^{pro}, compared to derivative **9a** bearing the unsubstituted phenethyl.

The concomitant introduction of a 2,4-dichlorophenoxy acetyl N-capping group and 2-substituted (derivatives **9i** and **9j**) or 2,4-disubstituted (**9f**) phenethyl at P1′ generally increased the potency against SARS-CoV-2 M^{pro}. Such derivatives might explore alternative conformations within the S1' pocket of SARS-CoV-2 M^{pro} (as observed for the co-crystal structure of **9e**) due to the presence of the 2,4-dichlorophenoxy acetyl N-capping group conferring a kinked conformation to the inhibitors.

On the contrary, the presence of the bulkier Met25 in S1′ of MERS M^{pro} might impair derivatives bearing the 2-substituted phenethyl moiety at P1′ from assuming alternative conformations, and thus explaining the preference for i) Cbz as N-capping group (**9c**) and ii) the combination of 2,4-dichlorophenoxy acetyl with smaller P1' groups, such as benzyl (**9d**).

2.3. Antiviral activity in Vero E6 cells against SARS-CoV-2 and cytotoxicity

In parallel, all the compounds were also tested in a phenotypic assays to evaluate their antiviral activity by CPE method against SARS-CoV-2 replicating in Vero E6 cells constitutively expressing GFP under the control of CMV promoter. All compounds were tested in dose response curves against viral replication and their EC_{50} values were determined (Table 2). Moreover, CC_{50} were measured in order to evaluate also their effect on cell viability and to calculate a selectivity index, by quantifying the viability as proportional to the GFP signal of untreated cells and expressed as $CC_{50.}$ ($SI = CC_{50}/EC_{50}$), indeed an antiviral agent should be able to selectively inhibit viral replication without causing cell toxicity. The compounds were tested alone but also in presence of the commercially available CP100356 (2 μM), that is a non toxic inhibitor of P-glycoprotein, an eukaryotic efflux pump highly expressed in Vero E6 cells. Indeed, drug efflux and the long cellular readout (72 h) might cause a reduction of intracellular inhibitor concentration and of its relative potency in cell-based assay, thus likely leading to underestimation of compound activity, as observed for similar peptidomimetic inhibitors of M^{pro} of human CoVs.

None of the compounds showed cytotoxicity either in absence or in presence of CP100356. In absence of CP100356, in the Vero-E6 phenotypic assay only **9a** seemed to be able to inhibit SARS-CoV-2 replication with an EC_{50} of 15.7 μM, while the other compounds with activity as SARS-CoV-2 M^{pro} inhibitors, were inactive. Worth noting, when tested with the P-gp inhibitor, almost all the compounds, with the only exception of derivative **9h**, rescued antiviral activity with **9d**, **9e**, **9f**, **9i** and **9j** displaying EC_{50} of 4.5, 8.0, 7.1 18.7 and 9.6 μM, respectively. In particular, compounds **9d** and **9e** showed also the most promising selectivity with SI values > 22 and >11, respectively. Conversely, the antiviral potency of **9a** did not change in presence of the P-glycoprotein inhibitor.

2.4. X-ray structures of SARS-CoV-2 M^{pro} bound with inhibitors

In order to confirm the docking prediction and the real formation of a covalent adduct with Cys145 of the α-ketoamide compounds we determined the crystal structures of SARS-Cov-2 M^{pro} in complex with the first synthesized inhibitors, **9a** and **9e**. Crystals with space group $P2_12_12_1$ containing one dimer per asymmetric unit were obtained by co-crystallization and seeding. The structures were solved at a resolution edge of 1,67 Å for M^{pro}- **9a** (PDB 7Q5E) and of 1,72 Å for M^{pro}- **9e** (PDB 7Q5F). Data collection and refinement statistics are listed in Supplementary Table S1.

In both complexed structures, the electron density of the active site of each protomer confirms the existence of similar adducts with a covalent binding between the α-keto carbon and the catalytic Cys145.

Indeed, the α-ketoamide inhibition mechanism involves the

formation of a tetrahedral thio-hemiketal adduct with *S*-configuration, able to mimic the hydrolysable amide bond of the natural substrate, through the nucleophilic addition of Cys145 to the 2-oxoamide moiety of the inhibitor in the catalytic site.

Overall, **9a** and **9e** show a comparable binding mode in the S1 and S2 pockets while they differ in positioning into S1' and S4 (Fig. 3A and B, and Fig. S2). As shown in Fig. 3, in both compounds the P1 γ-lactam moiety occupies the same position in S1, well fitting into the sub-pocket by forming hydrogen bonds with Glu166 and His163 side chains and with Phe140 main chain.

On the contrary, Cbz and 2,4 dicholorophenoxy acetyl groups orient at 120° one respect to the other: in **9a** the Cbz occupies the S4 pocket while in **9e** the 2,4 dicholorophenoxy acetyl points toward the solvent, leaving S4 pocket empty. Moreover, in the **9a** structure the electron density of the phenylethyl amino group clearly occupies the S1′ site having hydrophobic interactions with Thr25; the same moiety in **9e** could not be modeled in a unique conformation but flips over two positions: one inside the S1' site and one toward Thr26 and the 23–25 β-hairpin. Despite these differences, the active sites of the two structures are well superimposed (Fig. S3) not showing relevant movements in the side and main chains of the protein, with exclusion of the side chains of Met49 and M165 that have a displacement of less than 2 Å.

Notably, **9a** and **9e** have comparable potency in the biochemical assays suggesting that the main contribution to the enzyme inhibition is driven by covalent binding to Cys145 and by the good fitting of the central core of the two molecules.

2.5. Molecular modeling of 9c with SARS-CoV-2 M^{pro} and MERS-CoV M^{pro}

In order to investigate the potential binding mode of compound **9c**, the best dual inhibitor against SARS-CoV-2 and MERS M^{pro}, and to help interpretation of SAR data, we undertook docking studies using the CovDock workflow from Schrödinger [26].

Compound **9c** fits within the active site of the of SARS-CoV-2 M^{pro} similarly to the above-described compounds **9a** and **9e**. In agreement with the X-ray studies, the docked pose of **9c** showed the presence of the thio-hemiketal adduct in the *S* configuration, with the hydroxy group (formed by the nucleophilic attack of the active-site cysteine residue) accepting a hydrogen bond from His41, whereas the keto oxygen accepts two hydrogen bonds from the main chain amides of the oxyanion hole residues Gly143 and Cys145 (Fig. 4A). The P1 γ-lactam moiety is inserted into the S1 pocket, engaging the well-known interactions with Glu166 and His163 side chains and with Phe140 main chain. The Cbz cap formed a further H-bond with the NH of Glu166 main chain, as well as several hydrophobic interactions with Pro168, Ala191, and the aliphatic part of the side chain of Gln189. Finally, the P1′ group 2-methoxy phenethyl projects towards S1′ pocket, flanked by Thr25 and Thr26, resembling the alternative conformation assumed by the P1′ phenethyl group of **9e** (Fig. 4C). In this conformation, the 2-methoxy group is able to establish additional stabilizing hydrophobic interactions with Met49. The predicted binding mode of **9c** superimposes well with the co-crystallized ligand UAWJ246, with the proline P2 group of **9c** nicely fitting on the leucine P2 of UAWJ246 (Fig. 4D). The binding mode of compound **9c** was maintained also in MERS M^{pro} active site, with main differences observed in the orientation of the 2-methoxy group in the P1'; in fact, Thr25 in SARS-CoV-2 is replaced by a bulkier and hydrophobic methionine in MERS (Fig. 4B). This latter can form additional hydrophobic interactions with the P1′ fragment, which likely explain the general gain in potency towards MERS M^{pro} of ligands featuring 2-substituted phenethyl groups. As regards the cap group, it does not seem to greatly impact the inhibitory activity, however it could rather influence the pharmacokinetic properties of the compounds. Interestingly, the dichlorophenoxy acetyl cap group in **9e** X-ray structure is shifted downward, establishing intramolecular interactions with the P1 γ-lactam moiety; such conformation can be found in both the protomers of the X-ray structure. A similar situation has been observed also in the X-ray structures of other M^{pro} inhibitors, such as GC-376, UAWJ246 [27], which exist in a dynamic equilibrium between an "extended" conformation, stretching towards the S3 and S4 subsites, and a "kinked" conformation. Thus, the dichlorophenoxy acetyl cap might favor the equilibrium toward the kinked form, possibly stabilizing a more compact conformation of the ligand that could improve membrane permeation and enhance cellular activity. It is worth noting that very few investigations of the structural requirements of S1′ pocket have been reported. This pocket is characterized by one or more structured water molecules bridged to Thr26, as observed in several X-ray structures of inhibitors bound to M^{pro}, such as UAWJ246 [27], compound **11a** [13], nirmatrelvir [28]. The crystal structures of **9a** and **9e** reveal that these waters are conserved into the S1' pocket (Fig. S1, Supporting

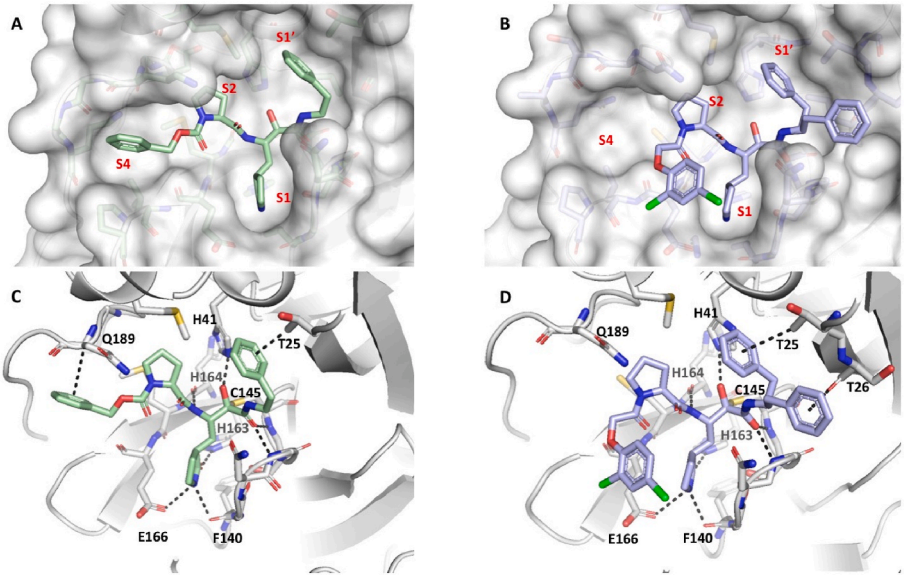

Fig. 3. Crystal structure of M^{pro} in complex with inhibitors **9a** and **9e**. Upper panels: Surface representation of the active site pocket with bound (A) **9a** (light green), and (B) **9e** (light blue). The P1–P4 and P1' moieties are labeled in red. Bottom panels: The key residues interacting with **9a** (C) and **9e** (D) in the active site pocket are displayed as white sticks and labeled.

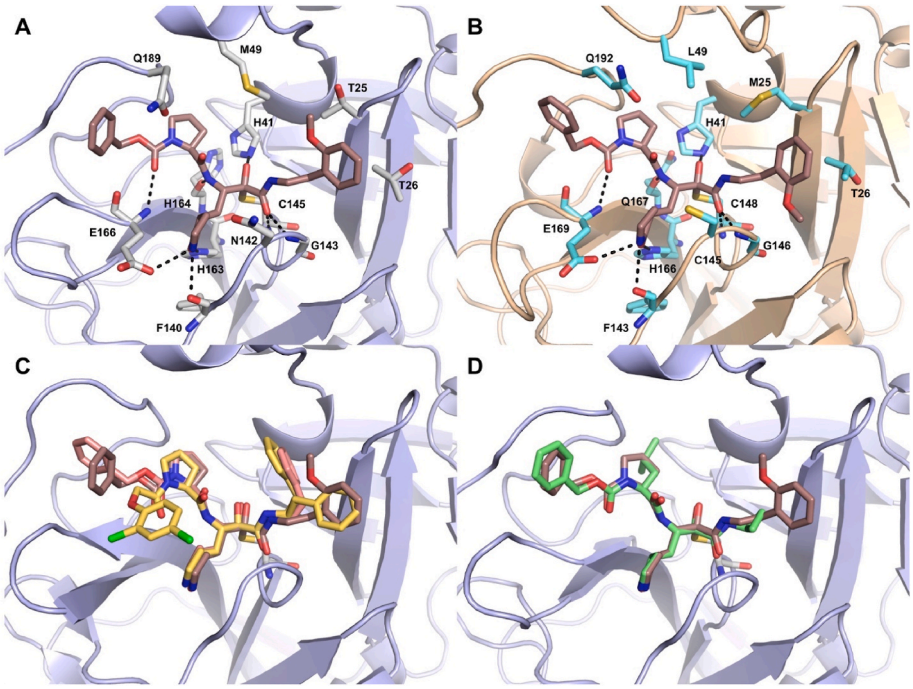

Fig. 4. Predicted binding mode of **9c** into SARS-CoV-2 (A, light-blue ribbons, PDB 6XBG) and MERS (B, wheat ribbons, PDB 4RSP) M^{pro}s. H-bonds discussed in the text are depicted as dashed black lines. (C) Overlay of **9c** docked pose (dirty-violet sticks) with **9a** and **9e** co-crystallized into SARS-CoV-2 M^{pro} (salmon and yellow sticks, PDB 7Q5E and 7Q5F respectively). (D) Overlay of **9c** docked pose (dirty-violet sticks) with UAWJ246 co-crystallographic pose (green sticks, PDB 6XBG).

Information); thus, the length and bulkiness of the phenethyl moiety do not cause waters displacement that might contribute to a potential reduction in inhibitory activity [29].

3. Conclusions

In order to explore a fast and efficient method to identify α−keto amide as novel covalent reversible of SARS-CoV-2 M^{pro}, the essential enzyme for virus replication and transcription, the PADAM oxidation route was optimized for this purpose providing an easy access to the α-ketoamide moiety.

The synthesized compounds proved to be good inhibitors of SARS-CoV-2 and MERS-CoV, with low nanomolar M^{pro} inhibitory activity, indicating their potential for further development as broad spectrum anti-coronaviral agents. In cell-based experiments, several compounds exhibited low micromolar antiviral activity. Molecular docking studies on key molecules **9a** and **9e**, predicted the binding mode and mechanism of action. Their co-crystal structures in complex with M^{pro} validated the in silico hypothesis and proved the expected formation of a tetrahedral thio-hemiketal adduct able to mimic the hydrolysable amide bond of the natural substrate. Furthermore, these structural data provide some additional consideration for the interaction between the P1′ moiety and S1' and foster further structure-based optimization for this newly conceived class of compounds.

4. Experimental section

4.1. Computational analyses

Protein and ligand preparation. The starting coordinates of SARS-CoV-2 M^{pro} in complex with compound UAWJ246 (PDB 6XBG), the α-ketoamide analog of GC-376 [27,30], as well as MERS M^{pro} in complex with compound **6** (PDB 4RSP) [31] were employed for the docking calculations. The proteins were processed through the Protein Preparation Wizard in Maestro (Schrödinger, LLC, New York, NY, 2021). X-ray water molecules were removed, the appropriate bond orders as well as charges and atom types were assigned, and the hydrogen atoms were added. The H-bond network was optimized by exhaustive sampling of rotamers, tautomers and protonation states of titratable amino acids at neutral pH. Finally, the protein structures were relaxed by means of a restrained minimization using the Impref module with the OPLS4 force field, by imposing a 0.3 Å RMSD limit from the initial coordinates as constraint. The chemical structures of compounds under study were built in Maestro from SMILES strings, before undergoing a ligand preparation workflow with LigPrep module (LigPrep, Schrödinger, LLC, New York, NY, 2021), predicting all tautomeric and protonation states at pH = 7 ± 2. The compounds were then energetically minimized using the OPLS4 force field.

Potential Binding Mode of Compounds in MERS-CoV and SARS-CoV-2 Main Proteases. For simulation of the covalent inhibition, the covalent docking (CovDock) workflow [26] from Schrödinger was used. The covalent reaction between the α-ketoamide group of the ligands and the M^{pro} catalytic cysteine residue (C145 in SARS-CoV-2 and C148 in MERS) was set up. The grid center was positioned at the centroid of the co-crystallized ligands; the pose prediction mode was employed, setting a minimization radius of 5.0 Å and ten poses for each ligand were generated. Final docked poses were selected on the basis of the scoring, the similarity to the co-crystallized ligand binding mode and the consistency of protein-ligand interactions with the experimental data. In order to ensure the reliability of the docking simulations, we investigated pose generation quality by re-docking of the co-crystalized ligands. The docking protocol well reproduced the experimental geometries, with root-mean-square deviation (RMSD) values of 0.41 and 1.30 Å for SARS-CoV-2 and MERS M^{pro}s, respectively.

4.2. Chemistry

General Experimental Procedures. Commercially available reagents and solvents were used without further purification; benzyl isocyanide (**5a**), phenethyl isocyanide (**5b**) and 1-(benzyloxycarbonyl) pyrrolidine-2-carboxylic acid (**4a**) were commercially available. Dichloromethane (DCM) was dried by distillation from P_2O_5 and stored

over activated molecular sieves (4 Å). When necessary the reactions were performed in oven-dried glassware under a positive pressure of dry nitrogen.

All the compounds were characterized by ^{1}H and ^{13}C attached proton test (APT) NMR spectra that were recorded at a Bruker Avance NEO instruments of 400 and 700 MHz. Mass spectra of final products were performed on LTQ Orbitrap XL™Fourier transform mass spectrometer (FTMS) equipped with an ESI ION MAX™ (Thermo Fisher, San José, USA) source operating in positive mode. The spectra were recorded by infusion into the ESI source using methanol (MeOH) as the solvent. High-resolution ESI-MS spectra were recorded using a Thermo LTQ Orbitrap XL mass spectrometer. The spectra were recorded by infusion into the ESI source using MeOH as the solvent. Chemical shifts (δ) are reported in parts per million (ppm) relative to the residual solvent peak. Column chromatography was performed on silica gel (70–230 mesh ASTM) using the reported eluents. Thin layer chromatography (TLC) was performed on 5 × 20 cm plates with a layer thickness of 0.25 mm (silica gel 60 F254). When necessary they were developed with ninidrin and $KMnO_4$. The purity of all compounds was confirmed by NMR and analytic HPLC-UV as ε4 92–95%.

General Preparation of Isocyanides 5 c-f. The substituted benzyl and phenethyl isocyanides were readily synthesized in two steps starting from the corresponding benzyl amines and phenethyl amines.

The formyl amides were obtained using 6.90 mmol of acetic anhydride and 8.1 mmol of formic acid at 60 °C for 3 h, in order to obtain the mixed anhydride. After cooling, this mixture was added slowly to a solution of the corresponding amine (3.0 mmol) in 5 mL of dry THF, in an ice bath. The reaction was stirred at room temperature until disappearance of the amine (usually 2 h). Then, the mixture was poured on ethyl acetate and the excess of the anhydride was destroyed by extraction with a saturate aqueous solution of sodium bicarbonate (3 × 50 mL). These formyl amides were used to generate the corresponding isocyanides.

To the formamide (3.34 mmol) dissolved in dry THF (5.56 mL) under N_2, dry triethylamine (3.12 mL; 22.4 mmol) was added, and the solution was cooled to 0 °C. Phosphorus oxychloride (531 μL, 5.68 mmol) was introduced to the reaction mixture dropwise over 10 min, and then stirring was continued for 1 h. After, Na_2CO_3 (ss) was added (pH = 8). The mixture was stirred vigorously for an additional 30 min8 and then transferred to a separatory funnel. The organic layer was separated and the aqueous phase extracted with additional CH_2Cl_2 (100 mL). The combined extracts were dried over $MgSO_4$ and evaporated, and the residue was purified by silica gel column chromatography, eluted with 5–10-20% Ethyl acetate/*n*-hexane.

5c: 2,4-dimethoxybenzyl isocyanide: pale yellow solid, 70% yield [32].

5d: 3-trifluoromethylbenzyl isocyanide: pale yellow oil, 84% yield [33].

5e: 2-fluorophenethyl isocyanide: pale yellow oil, 70% yield. ^{1}H NMR (DMSO-d_6, 400 MHz): ^{1}H NMR ($CDCl_3$, 400 MHz): δ 7.33–7.22 (m, 2H), δ 7.16–7.04 (m, 2H), δ 3.68–3.64 (m, 2H), δ 3.08–3.04 (m, 2H). ^{13}C APT ($CDCl_3$; 700 MHz): δ 161.18, 156.72, 131.28, 129.30, 128.55, 124.39, 115.49, 41.59, 29.51.

5f: 2-methoxyphenethyl isocyanide: pale yellow oil, 76% yield [34].

4.2.1. Preparation of the γ-lactam aldehyde (3)

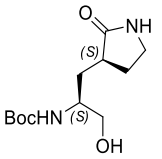

4.2.1.1. Tert-butyl (S)-1-hydroxy-3-((S)-2-oxopyrrolidin-3-yl)propan-2-yl carbamate (2). Lithium borohydride (189 mg; 8.7 mmol) was slowly added to a mixture of (S)-methyl 2-(tert-butoxycarbonylamino)-3-((*S*)-2-oxopyrrolidin-3-yl) propanoate (1) (500 mg; 1.75 mmol) in tetrahydrofuran (0.09 M) at 0 °C; reaction was then stirred at room temperature for 2 h5. Water was added and reaction was extracted with ethyl acetate (3 × 50 mL), dried with anhydrous sodium sulfate and evaporated. The crude material was purified using silica gel column chromatography (dichloromethane/methanol 95:5) to provide a white solid (240 mg; 53% yield).

^{1}HNMR (DMSO-d_6, 700 MHz): δ 7.55 (s, 1H), δ 6.57 (d, 1H, J = 9.1 Hz), δ 4.62 (t, 1 H, J = 5.6 Hz), δ 3.48–3.43 (m, 1H), δ3 3.36–3.33 (m, 1H), δ 3.25–3.22 (m, 1H), δ 3.18–3.11 (m, 2H), δ 2.23–2.15 (m, 2H), δ 1.71–1.67(m, 1H), δ 1.63–1.58 (m, 1H), δ 1.39 (s, 9H), δ 1.37–1.34 (m, 1H). ESI-MS (*m/z*): 315 $(M + H)^+$.

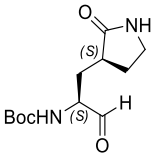

4.2.1.2. Tert-butyl (S)-1-oxo-3-((S)-2-oxopyrrolidin-3-yl)propan-2-yl carbamate (3). *Tert*-butyl (*S*)-1-hydroxy-3-((*S*)-2-oxopyrrolidin-3-yl) propan-2-ylcarbamate **1** (100 mg, 0,387 mmol) was dissolved in CH_2Cl_2 (1.9 mL), and then Dess−Martin periodinane (172 mg, 0.406 mmol) was added.

The resulting mixture was stirred at 20 °C for 1 h. The mixture was concentrated and purified by column chromatography on silica gel (CH_2Cl_2/MeOH = 97/3) to give **2** as a white solid (90 mg, 91% yield).[27]

4.2.2. Synthesis of N-substitued prolines (4a-c)

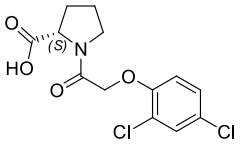

4.2.2.1. (S)-1-(2-(2,4-dichlorophenoxy)acetyl)pyrrolidine-2-carboxylic acid 4b. (*S*)-Methyl pyrrolidine-2-carboxylate hydrochloride (436 mg, 2.62 μμol), 2-(2,4 dichlorophenoxy) acetic acid (580 mg, 2.62 mmol), HATU (1.2 g, 3.14 mmol) and DIEA (1.01 g, 1.4 mL, 7.86 mmol) in anhydrous Dimethylformamide (15 mL) were stirred at 20 °C overnight. Water was added and reaction was extracted with dichloromethane (3 × 30 mL). The combined organic phases were washed with brine (2x), dried with anhydrous sodium sulfate and evaporated. The crude material was purified using silica gel column chromatography (*n*-hexane/ethylacetate 7:3) to furnish (*S*)-methyl 1-(2-(2,4-dichlorophenoxy) acetyl)pyrrolidine-2-carboxylate as light yellow solid (812 mg, 93% yield).

^{1}H NMR (DMSO-d_6, 400 MHz): δ7.57 (s, 1H), δ 7.35 (dd, 1H, J = 8.8 and 2.4 Hz), δ 7.01 (d, 1H, J = 8.8 Hz), δ4.98 (s, 2H), δ 4.35–4.30 (m, 1H), δ 3.64–3.57 (m, 5H), δ 2.22–2.13 (m, 1H), δ 1.99–1.92 (m, 2H), δ 1.88–1.82 (m, 1H).

Compound (*S*)-methyl 1-(2-(2,4-dichlorophenoxy)acetyl)pyrrolidine-2-carboxylate (300 mg, 0.90 mmol) was dissolved in tetrahydrofuran (4.5 mL) and a solution of lithium hydroxide(65 mg, 2.71 mmol) in water (1.5 mL) was slowly added. The reaction was stirred at 20 °C for 1.5 h. Then, 1 M HCl was added to the reaction solution until pH 2. Then the reaction mixture was extracted with 90 mL of Ethyl acetate (3 × 30 mL), and the organic layer was washed with 50 mL of brine and dried

over anhydrous Na_2SO_4. The solvent was evaporated to dryness and the product **4b** was used for the next step without further purification (286 mg, quantitative). ^{1}H NMR (DMSO-d_6, 400 MHz): δ 12.5 (bs, 1H), δ 7.57 (s, 1H), δ7.31 (dd, 1H, J = 8.8 and 2.4 Hz), δ7.02 (d, 1H, J = 9.2 Hz), δ 4.96 (s, 2H), δ 4.27–4.24 (m, 1H), δ 3.61–3.55 (m, 2H), δ 2.18–2.13 (m, 1H), δ 1.96–1.91 (m, 2H), δ 1.89–1.82 (m, 1H).

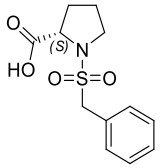

4.2.2.2. (S)-1-(benzylsulfonyl)pyrrolidine-2-carboxylic acid 4c. Methyl pyrrolidine-2-carboxylate hydrochloride (300 mg, 1.81 mmol) was dissolved in anhydrous dichloromethane (3.5 mL) at 0 °C. To this solution, phenylmethane sulfonylchloride (345 mg, 1.81 mmol), and TEA (549.5 g, 757 μL, 5.43 mmol) were added and reaction was stirred at 20 °C for 1 h. Water was then added and reaction was extracted with ethyl acetate (2 × 50 mL). The combined organic phases were washed with 50 mL of brine, dried over anhydrous Na_2SO_4 and evaporated. The crude material was purified using silica gel column chromatography (*n*-hexane/ethyl acetate 8:2) to furnish (*S*)-methyl 1-(benzylsulfonyl)pyrrolidine-2-carboxylate as light yellow solid (444 mg, 86% yield).

^{1}H NMR (DMSO-d_6, 400 MHz): δ 7.45–7.36 (m, 5H), δ 4.55–4.45 (m, 2H), δ 4.16–4.13 (m, 1H), δ 3.64 (s, 3H), δ 3.29–3.23 (m, 2H), δ 2.16–2.10 (m, 1H), δ 1.91–1.80 (m, 3H).

(*S*)-methyl 1-(benzylsulfonyl)pyrrolidine-2-carboxylate (440 mg, 1.55 mmol) was dissolved in tetrahydrofuran (7.75 mL) and a solution of lithium hydroxide (112 mg, 4.66 mmol) in water (2.6 mL) was slowly added. The reaction was stirred at 20 °C for 1.5 h. Then, 1 M HCl was added to the reaction solution until pH = 2. Then the reaction mixture was extracted with 90 mL of Ethyl acetate (3 × 30 mL), and the organic layer was washed with 50 mL of brine and dried over anhydrous Na_2SO_4. The solvent was evaporated to dryness and the product **4c** was used for the next step without further purification (400 mg, 96% yield).

^{1}H NMR (DMSO-d_6, 400 MHz): δ 12.7 (bs, 1H), δ 7.45–7.36 (m, 5H), δ 4.54–4.43 (m, 2H), δ 4.07–4.04 (m, 1H), δ 3.29–3.18 (m, 2H), δ 2.15–2.09 (m, 1H), δ 1.89–1.80 (m, 3H).

4.2.3. General procedure for the synthesis of Passerini adducts (6a-j)

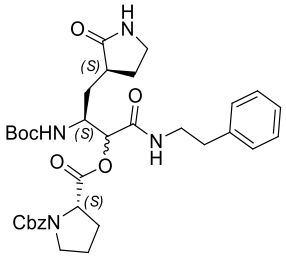

4.2.3.1. ***(S)-1-benzyl2-((S)-3-(tert-butoxycarbonylamino)-1-oxo-4-((S)-2-oxopyrrolidin-3-yl)-1-(phenethylamino)butan-2-yl) pyrrolidine-1,2-dicarboxylate) 6a.*** A mixture of *tert*-butyl (*S*)-1-oxo-3-((*S*)-2-oxopyrrolidin-3-yl)propan-2-ylcarbamate **(3)** (95 mg, 0.37 mmol), (*S*)-1-(benzyloxycarbonyl)pyrrolidine-2-carboxylic acid (101 mg, 0.41 mmol) and phenylethyl isocyanide (54 mg, 56 μL, 0.41 mmol) in dichloromethane (0.35 M) was stirred overnight at room temperature. The mixture was concentrated and purified by column chromatography on silica gel (CH_2Cl_2/MeOH = 98/2) to give the 6a as off white solid (200 mg, 85% yield, mixture of 2 diasteroisomers).

^{1}H NMR (DMSO-d_6, 400 MHz): δ 7.54 (t, J = 5.2 Hz, 1 H), δ 7.38–7.26 (m, 8H), δ 7.21–7.18 (m, 3H), δ 6.13, 6.07 (2 m, 1H), δ 5.57–5.49 (m, 1H), δ 5.26–5.08 (m, 2H), δ 4.44–4.18 (m, 2H), δ 3.65–3.30 (m, 6H), δ 2.91–2.76 (m, 2H), δ 2.57–2.42 (m, 2H), δ 2.30–1.79 (m, 7H), δ 1.44,1.43 (2s, 9H).

ESI-MS (*m/z*): 637.3 $[M + H]^+$, 659.2 $[M + Na]^+$, 675.4 $[M + K]^+$

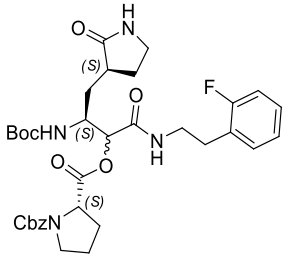

4.2.3.2. ***(S)-1-benzyl2-((S)-3-(tert-butoxycarbonylamino)-1-(2-fluorophenethylamino)-1-oxo-4-((S)-2-oxopyrrolidin-3-yl)butan-2-yl) pyrrolidine-1,2-dicarboxylate) 6b.*** Compound **6b** was prepared according to 6a, using **3**, 1((benzyloxy)carbonyl)pyrrolidine-2-carboxylic acid and 2-fluorophenethyl isocyanide (**5e**). Silica gel column chromatography (CH_2Cl_2/MeOH = 95/5). White solid (71 mg, 64% yield) ^{1}H NMR, LC/MS and HRMS- See supplementary material.

ESI-MS (*m/z*): 655.3 $[M + H]^+$, 654.1 $[M + Na]^+$, 693.5 $[M + K]^+$

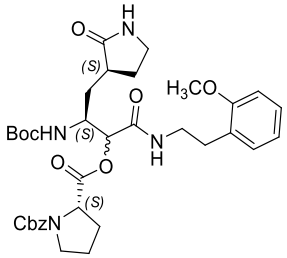

4.2.3.3. (S)-1-benzyl2-((S)-3-(tert-butoxycarbonylamino)-1-(2-methoxyphenethylamino)-1-oxo-4-((S)-2-oxopyrrolidin-3-yl)butan-2-yl) pyrrolidine-1,2-dicarboxylate 6c. Compound **6c** was prepared according to 6a, using **3**, 1((benzyloxy)carbonyl)pyrrolidine-2-carboxylic acid and 2-methoxyphenethyl isocyanide (**5f**). Silica gel column chromatography (CH_2Cl_2/MeOH = 95/5). White solid (97 mg, 66% yield) ^{1}H NMR, LC/MS and HRMS- See supplementary material.

ESI-MS (*m/z*): 668.3 $[M + H]^+$, 689.5 $[M + Na]^+$, 705.5 $[M + K]^+$

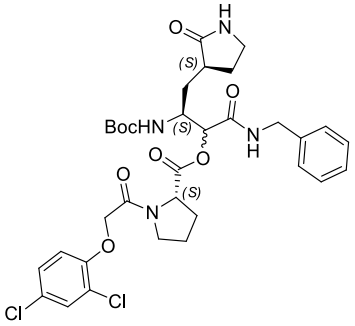

4.2.3.4. ***(S)-((S)-1-(benzylamino)-3-(tert-butoxycarbonylamino)-1-oxo-4-((S)-2-oxopyrrolidin-3-yl)butan-2-yl)1-(2-(2,4-dichlorophenoxy)acetyl) pyrrolidine-2-carboxylate) 6d.*** A mixture of **3** (31 mg, 0.12 mmol), **4b** (42 mg, 0.13 mmol) and benzyl isocyanide (15 mg,

16 μL, 0.13 mmol) in dichloromethane (0.34 mL) was stirred at room temperature overnight. The mixture was concentrated and purified by column chromatography on silica gel (CH_2Cl_2/MeOH = 97/3) to give the **6d** as an off white solid (54 mg, 65% yield, mixture of 2 diasteroisomers) ^{1}H NMR, LC/MS and HRMS- See supplementary material.

ESI-MS (*m/z*): 692.1 [M + H]$^+$, 713.4 [M +Na] $^+$, 729.4 [M + K] $^+$

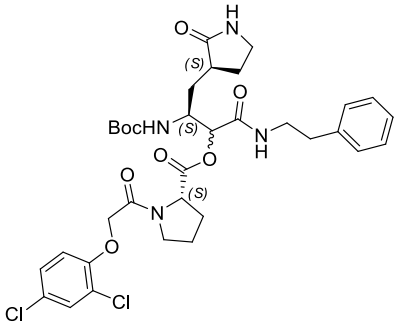

4.2.3.5. (S)-((S)-3-(tert-butoxycarbonylamino)-1-oxo-4-((S)-2-oxopyrrolidin-3-yl)-1-(phenethylamino)butan-2-yl)1-(2-(2,4-dichlorophenoxy) acetyl)pyrrolidine-2-carboxylate 6e. Compound **6e** was prepared according to **6d** starting from 3, 4b and phenylethyl isocyanide. Silica gel column chromatography (CH_2Cl_2/MeOH = 97/3). White solid (71.5 mg, 72% yield, mixture of 2 diasteroisomers).

ESI-MS (*m/z*): 706.1 [M + H]$^+$, 727.3 [M +Na] $^+$, 743.3 [M + K] $^+$

^{1}H NMR (DMSO-d_6, 400 MHz): δ 8.37, 7.99 (2t, 1H, J = 6.4 Hz, J = 5.6 Hz), δ 7.65–7.50 (m, 2H), δ 7.36–7.11 (m, 6H), δ 7.05–6.96 (m, 1H), δ 6.83, 6.72 (2d, 1H, J = 9.2 Hz, J = 10 Hz), δ 5.02, 4.85 (2d, 2H, J = 6.0 Hz, J = 5.0 Hz), δ 4.49–4.45 (m, 1H), δ 4.02–3.86 (m, 1H), δ 3.72–3.57 (m, 3H), δ 3.21–3.08 (m, 5H), δ 2.68–2.67 (m, 1H), δ 2.61 (t, 2H, J = 7.6 Hz), δ 2.34–2.32 (m, 1H), δ 2.28–1.8 (m, 6H), δ 1.36,1.35 (2s, 9H).

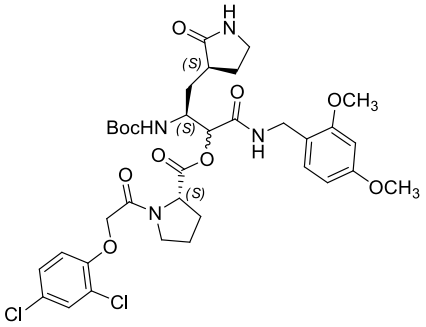

4.2.3.6. (S)-((S)-3-(tert-butoxycarbonylamino)-1-(2,4-dimethoxybenzylamino) -1-oxo-4-((S)-2-oxopyrrolidin-3-yl)butan-2-yl)1-(2-(2,4 dichlorophenoxy)acetyl)pyrrolidine-2-carboxylate 6f. Compound **6f** was prepared according to **6d** starting from 3, 4b and 2,4-dimethoxybenzyl isocyanide (5c). Silica gel column chromatography (CH_2Cl_2/MeOH = 97/3). White solid (57 mg, 69% yield, mixture of 2 diasteroisomers) ^{1}H NMR, LC/MS and HRMS- See supplementary material.

ESI-MS (*m/z*): 752.1 [M + H]$^+$, 773.3 [M +Na] $^+$, 789.3 (M + K]$^+$

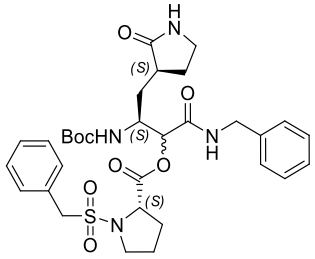

4.2.3.7. (S)-((S)-1-(benzylamino)-3-(tert-butoxycarbonylamino)-1-oxo-4-((S)-2-oxopyrrolidin-3-yl)butan-2-yl) 1-(benzylsulfonyl)pyrrolidine-2-carboxylate 6g. Compound **6g** was prepared according to **6d** starting from 3, 4c and benzyl isocyanide. Silica gel column chromatography (CH_2Cl_2/MeOH = 97/3). White solid (51 mg, 72% yield, mixture of 2 diasteroisomers).

^{1}H NMR, LC/MS and HRMS- See supplementary material.

ESI-MS (*m/z*): 643.1 [M + H]$^+$, 665.3 [M +Na] $^+$, 681.3[M + K] $^+$

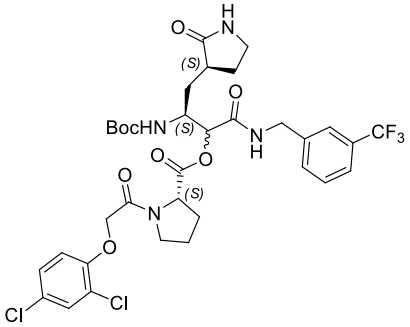

4.2.3.8. (S)-((S)-3-(tert-butoxycarbonylamino)-1-oxo-4-((S)-2-oxopyrrolidin-3-yl)-1-(3-(trifluoromethyl)benzylamino)butan-2-yl) 1-(2-(2,4-dichlorophenoxy)acetyl)pyrrolidine-2-carboxylate 6h. Compound **6h** was prepared according to 6d starting from 3, 4b and 3-(trifluoromethyl) benzyl isocyanide (5d). Silica gel column chromatography (CH_2Cl_2/MeOH = 98/2). White solid (52 mg, 63% yield, mixture of 2 diasteroisomers) ^{1}H NMR, LC/MS and HRMS- See supplementary material.

ESI-MS (*m/z*): 760.1 [M + H]$^+$, 781.3 [M +Na] $^+$, 798.3 [M + K] $^+$

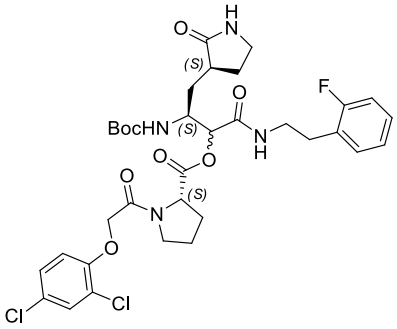

4.2.3.9. (S)-((S)-3-(tert-butoxycarbonylamino)-1-(2-fluorophenethylamino)-1-oxo-4-((S)-2-oxopyrrolidin-3-yl)butan-2-yl) 1-(2-(2,4-dichlorophenoxy) acetyl)pyrrolidine-2-carboxylate 6i. Compound **6i** was prepared according to 6d starting from 3, 4b and 2-fluorophenethyl isocyanide (5e). Silica gel column chromatography (CH_2Cl_2/MeOH = 95/5). White solid (69 mg, 61% yield, mixture of 2 diasteroisomers) ^{1}H NMR, LC/MS and HRMS- See supplementary material.

ESI-MS (*m/z*): 723.2 [M + H]$^+$, 745.4 [M +Na] $^+$, 762.4 [M + K] $^+$

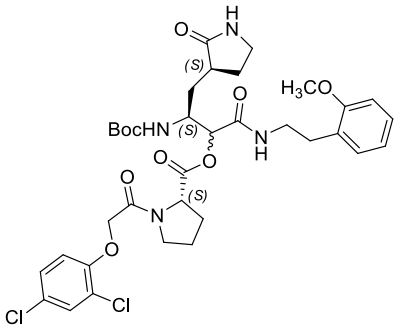

4.2.3.10. (S)-((S)-3-(tert-butoxycarbonylamino)-1-(2-methoxyphenethylamino)-1-oxo-4-((S)-2-oxopyrrolidin-3-yl)butan-2-yl)1-(2-(2,4-dichlorophenoxy) acetyl)pyrrolidine-2-carboxylate 6j. Compound **6j** was prepared according to 6d starting from 3, 4b and 2-methoxyphenethyl isocyanide (5f).

Silica gel column chromatography (CH_2Cl_2/MeOH = 95/5). White solid (100 mg, 65% yield, mixture of 2 diasteroisomers) ^{1}H NMR, LC/MS and HRMS- See supplementary material.

ESI-MS (*m/z*): 735.2 $[M + H]^+$, 757.4 $[M + Na]^+$, 773.4$[M + K]^+$

4.2.4. General procedure for α-ketoamides 9a-j

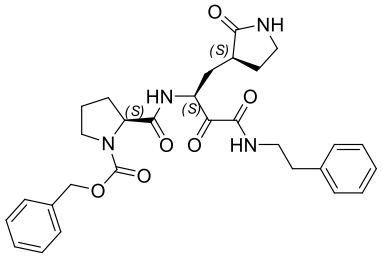

4.2.4.1. (S)-benzyl2-((S)-3,4-dioxo-1-((S)-2-oxopyrrolidin-3-yl)-4-(phenethylamino)butan-2ylcarbamoyl)pyrrolidine-1-carboxylate 9a. Compound 6a (0.16 mmol) was dissolved in dichloromethane (1.2 mL), then trifluoroacetic acid (0.4 mL) was added. The reaction was stirred at room temperature for 1 h and monitored through a (positive) ninidrine test. After removal of trifluoroacetic acid with diethyl ether, dichloromethane (0.7 mL) and triethylamine (0.2 mL) were added and the mixture was stirred overnight. The ninidrine test resulted negative and a saturated solution of NaCl was then added and the mixture was extracted with dichloromethane (3 × 20 mL), dried with anhydrous sodium sulfate and evaporated in vacuo. The crude was then dissolved in CH_2Cl_2 (0.7 mL), and then Dess Martin periodinane (63 mg, 0.15 mmol) was added.

The resulting mixture was stirred at 20 °C for 1 h. The mixture was concentrated and purified by column chromatography on silica gel (CH_2Cl_2/MeOH = 95/5) to give compound **9a** (40 mg; 0.075 mmol; 73% yield) as white solid. ^{1}H NMR (DMSO-d_6, 400 MHz): δ 8.78–8.74 (m, 1H), δ 8.58–8.53 (m, 1 H), δ 7.65–7.63 (d, 1 H, J = 4.8 Hz), δ 7.37–7.26 (m, 7H), δ 7.20–7.16 (m, 2H), δ 5.06–4.91 (m, 3 H), δ 4.32–4.23 (m, 1H), δ 3.51–3.36 (m, 3H), δ 3.17–3.04 (m, 2H), δ 2.95–2.89 (m, 1 H), δ 2.79–2.75 (m, 2H), δ 2.44–2.34 (m, 1H), δ 2.21–2.06 (m, 2 H), δ 1.85–1.77 (m, 4H), δ 1.68–1.46 (m, 2H). ^{13}C APT (DMSO-d_6; 400 MHz): δ 197.0, 178.4, 172.9, 161.1, 154.2, 139.5, 137.5, 129.1, 128.8, 128.7, 128.2, 128.0, 127.8, 127.3, 126.6, 66.2, 59.3, 52.6, 47.5, 38.1, 35.0, 31.6, 30.5, 27.4, 24.3, 23.4, 22.5.

ESI-MS (*m/z*): 535.4 $[M + H]^+$

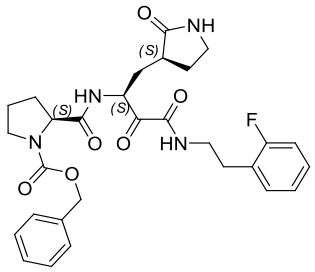

4.2.4.2. (S)-benzyl2-((S)-4-(2-fluorophenethylamino)-3,4-dioxo-1-((S)-2-oxopyrrolidin-3-yl)butan-2-ylcarbamoyl)pyrrolidine-1-carboxylate 9b. White solid, 76% yield; ^{1}H NMR (DMSO-d_6, 400 MHz): δ 8.82–8.79 (m, 1H), δ 8.57–8.52 (m, 1H), δ 7.64 (d, 1H, J = 5.2 Hz), δ 7.37–7.24 (m, 7H), δ 7.16–7.09 (m, 2H), δ 5.06–4.91 (m, 3H), δ 4.32–4.22 (m, 1H), δ 3.47.3.35 (m, 4H), δ 3.14–3.04 (m, 2H), δ 2.85–2.75 (m, 2H), δ 2.20–2.06 (m, 3H), δ 1.86–1.76 (m, 4H), δ 1.65–1.44 (m, 2H). ^{13}C APT (DMSO-d_6, 700 MHz): δ 197.0, 178.3, 173.0, 161.9,161.1, 154.2, 137.5, 131.7, 128.9, 128.8, 128.2, 128.0, 127.8, 127.3, 126.0, 124.8, 115.6, 66.2, 59.3, 52.7, 47.5, 46.9, 38.2, 31.6, 30.5, 28.5, 27.3, 24.3, 23.4.

ESI-MS (*m/z*): 553.4 $[M + H]^+$

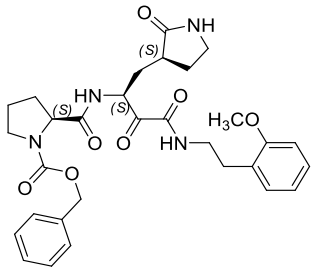

4.2.4.3. (S)-benzyl2-((S)-4-(2-methoxyphenethylamino)-3,4-dioxo-1-((S)-2-oxopyrrolidin-3-yl)butan-2-ylcarbamoyl)pyrrolidine-1-carboxylate 9c. White solid, 73% yield; ^{1}H NMR (DMSO-d_6, 400 MHz): δ 8.60–8.67 (m, 1H), δ 8.57–8.52 (m, 1H), δ 7.64 (d, 1H, J = 5.2 Hz), δ 7.37–7.27 (m, 5H), δ 7.18 (t, 1H, J = 7.6 Hz), δ 7.12–7.08 (m, 1H), δ 6.94 (d, 1H, J = 8.0 Hz), δ 6.84 (t, 1H, J = 7.2 Hz), δ 5.06–4.93 (m, 3H), δ 4.32–4.22 (m, 1H), δ 3.75 (s, 3H), δ 3.48.3.27 (m, 4H), δ 3.18–3.06 (m, 2H), δ 2.97–2.89 (m, 1H), δ 2.79–2.71 (m, 2H), δ 2.20–2.07 (m, 2H), δ 1.88–1.76 (m, 4H), δ 1.65–1.47 (m, 2H). ^{13}C APT (DMSO-d_6, 700 MHz): δ 197.2, 178.3, 172.9, 161.1, 157.7, 137.5, 130.4, 128.8, 128.2, 120.7, 111.1, 66.2, 59.9, 59.3, 55.7, 52.8, 47.5, 47.0, 38.2, 31.6, 30.5, 29.8, 27.4, 23.4.

ESI-MS (*m/z*): 565.4 $[M + H]^+$, 587.5 $[M + Na]^+$

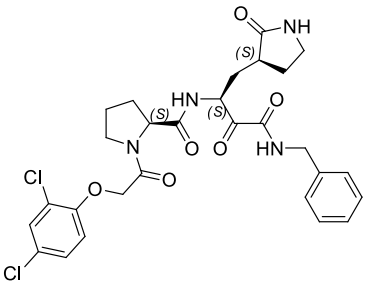

4.2.4.4. (S)–N-((S)-4-(benzylamino)-3,4-dioxo-1-((S)-2-oxopyrrolidin-3-yl)butan-2-yl)-1-(2-(2,4-dichlorophenoxy)acetyl)pyrrolidine-2-carboxamide 9d. White solid, 41% yield; ^{1}H NMR (DMSO-d_6, 400 MHz): δ 9.20

(t, 1H, $J = 6.8$ Hz), δ 8.58 (d, 1 H, $J = 7.2$ Hz), δ 7.60 (s, 1 H), δ 7.56–7.55 (m, 1H), δ 7.34–7.23 (m, 6H), δ 7.10–7.07 (d, 1H, $J = 8.8$ Hz), δ 4.96 (d, CH2, 2H, $J = 6.0$ Hz), δ 4.92–4.87 (m, 1 H), δ 4.33–4.28 (m, 3H), δ 3.62–3.57 (m, 1H), δ 3.52–3.48 (m, 1H), δ 3.09–3.04 (m, 1 H), δ 2.93–2.87 (m, 1H), δ 2.38–2.30 (m, 1H), δ 2.18–2.10 (m, 1H), δ 2.03–1.84 (m, 4H), δ 1.80–1.55 (m, 3H). ^{13}C APT (DMSO-d_6, 700 MHz): δ 197.7, 178.7, 172.3, 165.8, 161.7, 153.0, 139.0, 129.5, 128.6, 128.1, 127.8, 127.3, 124.8, 115.7, 66.9, 59.8, 53.8, 52.7, 46.0, 42.5, 37.8, 31.4, 29.5, 27.8, 24.6.

ESI-MS (m/z): 589.3 $[M+H]^+$, 611.4 $[M+ Na]^+$

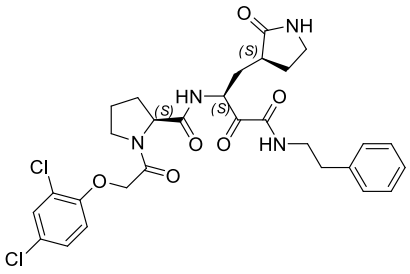

4.2.4.5. (S)-1-(2-(2,4-dichlorophenoxy)acetyl)-N-((S)-3,4-dioxo-1-((S)-2-oxopyrrolidin-3-yl)-4-(phenethylamino)butan-2-yl)pyrrolidine-2-carboxamide 9e. White solid, 40% yield; ^{1}H NMR (DMSO-d_6, 400 MHz): δ 8.73 (t, 1 H, $J = 5.6$ Hz), δ 8.53 (d, 1 H, $J = 7.2$ Hz), δ 7.60 (s, 1H), δ 7.55–7.54 (m, 1H), δ 7.31–7.25 (m, 3H), δ 7.21–7.17 (m, 3H), δ 7.06 (d, 1H, $J = 8.8$ Hz), δ 5.01–4.90 (m, 3H), δ 4.34–4.31 (m, 1H), δ 3.63–3.57 (m, 1H), δ 3.54–3.47 (m, 1H), δ 3.10–3.05 (m, 1 H), δ 2.98–2.87 (m, 1H), δ 2.80–2.73 (m, 3H), δ 2.36–2.30 (m, 1H), δ 2.15–2.00 (m, 3H), δ 1.93–1.79 (m, 4H), δ 1.65–1.48 (m, 2H). ^{13}C APT (DMSO-d_6, 700 MHz): δ 197.2, 178.7, 172.1, 165.9, 161.7, 153.1, 139.5, 129.5, 129.1, 128.8, 128.1, 124.9, 122.4, 115.8, 66.8, 59.8, 52.5, 45.9, 37.9, 35.0, 31.5, 29.5, 27.7, 24.7.

ESI-MS (m/z): 603.2$[M +H]^+$, 625.4 $[M + Na]^+$

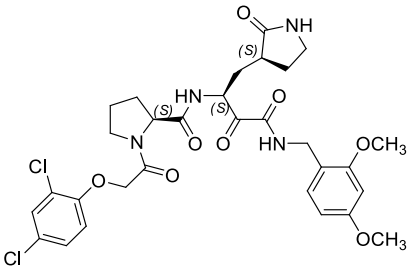

4.2.4.6. (S)-1-(2-(2,4-dichlorophenoxy)acetyl)-N-((S)-4-(2,4-dimethoxybenzylamino)-3,4-dioxo-1-((S)-2-oxopyrrolidin-3-yl)butan-2-yl)pyrrolidine-2-carboxamide 9f. White solid, 29% yield; ^{1}H NMR (DMSO-d_6, 400 MHz): δ 8.83 (t, 1H, $J = 6.4$ Hz), δ 8.56 (d, 1H, $J = 7.2$ Hz), δ 7.60 (s, 1H), δ 7.56–7.55 (m, 1H), δ 7.30–7.28 (m, 1H), δ 7.08–7.00 (m, 2H), δ 6.55–6.53 (m, 1H), δ 6.48–6.45 (m, 1H), δ 5.00–4.88 (m, 3H), δ 4.33–4.30 (m, 1H), δ 4.22 (d, 2H, $J = 6.0$ Hz), δ 3.79 (s, 3H, CH3), δ 3.74 (s, 3H, CH_3), δ 3.63–3.57 (m, 1H), δ 3.52–3.47 (m, 1H), δ 3.09–3.03 (m, 1H), δ 2.93–2.86 (m, 1H), δ 2.37–2.30 (m, 1H), δ 2.18–2.09 (m, 1H), δ 2.05–1.98 (m, 1H), δ 1.95–1.85 (m, 3 H), δ 1.79–1.69 (m, 2H), δ 1.62–1.55 (m, 1H). ^{13}C APT (DMSO-d_6, 700 MHz): δ 197.3, 178.8, 172.1, 165.8, 161.9, 160,2, 158.0, 153.2, 135.6, 129.5, 128.9, 128.1, 127.0, 124.9, 122.4, 118.3, 115.8, 104.8, 98.6, 66.8, 59.8, 55.9, 55.7, 52.6, 45.9, 37.3, 31.4, 29.5, 27.8, 24.7.

ESI-MS (m/z): 649.2$[M + H]^+$, 671.2 $[M + Na^+]$.

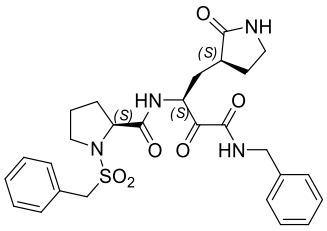

4.2.4.7. (S)–N-((S)-4-(benzylamino)-3,4-dioxo-1-((S)-2-oxopyrrolidin-3-yl)butan-2-yl)-1-(benzylsulfonyl)pyrrolidine-2-carboxamide 9g. White solid, 19% yield; ^{1}H NMR (DMSO-d_6, 400 MHz): δ 9.22 (t, 1H, $J = 6.4$ Hz), δ 8.60 (d, 1H, $J = 7.2$ Hz), δ 7.67 (s, 1H), δ 7.45–7.43 (m, 2H), δ 7.40–7.37 (m, 3H), δ 7.33–7.22 (m, 5H),δ 5.01–4.96 (m, 1H), δ 4.51–4.41 (m, 2 H), δ 4.33–4.26 (m, 2H), δ 4.23–4.19 (m, 1H), δ 3.28–3.07 (m, 4H), δ 2.40–2.33 (m, 1H), δ 2.27–2.14 (m, 2H), δ 2.09–2.00 (m, 2H), δ 1.84–1.74 (m, 3H), δ 1.72–1.62 (m, 1H). ^{13}C APT (DMSO-d_6, 700 MHz): δ 196.9, 178.7, 172.5, 161.5, 139.0, 135.6, 132.2, 131.4, 130.2, 128.7, 127.8, 127.4, 127.0, 62.2, 61.4, 55.4, 53.0, 49.2, 42.5, 38.1, 31.6, 27.8, 24.8.

ESI-MS (m/z): 541.3 $[M + H]^+$, 563.3 $[M+ Na]^+$

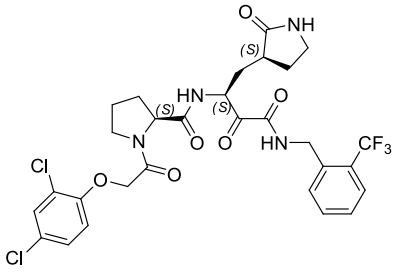

4.2.4.8. (S)-1-(2-(2,4-dichlorophenoxy)acetyl)-N-((S)-3,4-dioxo-1-((S)-2-oxopyrrolidin-3-yl)-4-(2-(trifluoromethyl)benzylamino)butan-2-yl)pyrrolidine-2-carboxamide 9h. White solid; 27% yield.

^{1}H NMR (DMSO-d_6, 400 MHz): δ 9.29 (t, 1H, $J = 6.4$ Hz), δ 8.60 (d, 1H, $J = 7.2$ Hz), δ 7.64–7.55 (m, 6 H), δ 7.30–7.27 (m, 1H), δ 7.08 (d, 1H, $J = 8.8$ Hz), δ 5.00–4.84 (m, 3H), δ 4.41–4.28 (m, 3H), δ 3.62–3.56 (m, 1H), δ 3.53–3.45 (m, 1H), δ 3.12–3.03 (m, 1H), δ 2.93–2.87 (m, 1H), δ 2.34–2.30 (m, 1H), δ 2.18–2.11 (m, 1H), δ 2.00–1.95 (m, 2H), δ 1.88–1.80 (m, 2H), δ 1.72–1.66 (m, 2H), δ 1.61–1.54 (m, 1H). ^{13}C APT (DMSO-d_6, 700 MHz): δ 197.0, 178.8, 172.1, 165.9, 162.0, 153.2, 140.5, 135.6, 132.0, 129.9, 129.5, 128.1, 127.0, 124.9, 124.5, 124.2, 122.4, 115.8, 66.9, 59.8, 52.7, 45.9, 42.1, 40.5, 37.8, 31.4, 29.4, 27.8, 24.6.

ESI-MS (m/z): 657.3 $[M + H]^+$, 679.3$[M + Na]^+$

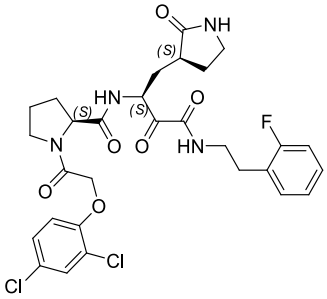

4.2.4.9. (S)-1-(2-(2,4-dichlorophenoxy)acetyl)-N-((S)-4-(2-fluorophenethylamino)-3,4-dioxo-1-((S)-2-oxopyrrolidin-3-yl)butan-2-yl)pyrrolidine-2-carboxamide 9i. White solid, 60% yield; ^{1}H NMR (DMSO-d_6,

400 MHz): δ 8.79 (t, 1H, $J = 6.0$ Hz), δ 8.53 (d, 1H, $J = 7.6$ Hz), δ 7.61 (s, 1H), δ 7.56–7.54 (m, 1H), δ 7.31–7.22 (m, 3H), δ 7.15–7.09 (m, 2H), δ 7.06 (d, 1H, $J = 9.2$), δ 5.00–4.88 (m, 3H), δ 4.34–4.31 (m, 1H), δ 3.63–3.58 (m, 1H), δ 3.53–3.47 (m, 1H), δ 3.43–3.29 (m, 2H), δ 3.13–3.05 (m, 1H), δ 2.97–2.87 (m, 1H), δ 2.87–2.75 (m, 3H), δ 2.36–2.28 (m, 1H), δ 2.15–2.00 (m, 3H), δ 1.94–1.75 (m, 3H), δ 1.61–1.45 (m, 1H). ^{13}C APT (DMSO-d_6, 700 MHz): δ 197.1, 178.7, 172.2, 165.8, 161.6, 160.5, 153.2, 135.6, 131.6, 131.2, 129.5, 128.8, 128.1, 127.0, 124.8, 122.4, 115.6, 66.8, 62.2, 59.8, 52.5, 45.9, 39.1, 37.9, 31.5, 29.6, 28.5, 27.7, 24.7.

ESI-MS (*m/z*): 621.3[M + H]$^+$, 643.4[M + Na]$^+$

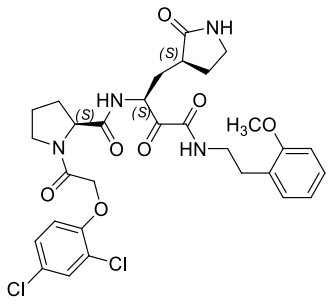

4.2.4.10. (S)-1-(2-(2,4-dichlorophenoxy)acetyl)-N-((S)-4-(2-methoxyphenethylamino)-3,4-dioxo-1-((S)-2-oxopyrrolidin-3-yl)butan-2-yl)pyrrolidine-2-carboxamide 9j. White solid, 61% yield; ^{1}H NMR (DMSO-d_6, 400 MHz): δ 8.67 (t, 1H, $J = 6$ Hz), δ 8.53 (d, 1H, $J = 7.6$ Hz), δ 7.61 (s, 1H), δ 7.56–7.54 (m, 1H), δ 7.31–7.28 (m, 1H), δ 7.22–7.16 (m, 1H), δ 7.12–7.01 (m, 2H), δ 6.97–6.93 (m, 1H), δ 6.88–6.82 (m, 1H), δ 5.01–4.89 (m, 3H), δ 4.34–4.31 (m, 1H), δ 3.78 (s, 3H), δ 3.63–3.57 (m, 1H), δ 3.53–3.46 (m, 1H), δ 3.17 (d, 1H, $J = 5.2$), δ 3.10–3.04 (m, 1H), δ 2.98–2.96 (m, 1H), δ 2.93–2.86 (m, 1H), δ 2.77–2.71 (m, 3H), δ 2.36–2.28 (m, 1H), δ 2.15–2.00 (m, 2H), δ 1.92–1.77 (m, 3H), δ 1.60–1.47 (m, 2H).

^{13}C APT (DMSO-d_6, 700 MHz): δ 197.3, 178.8, 172.1, 165.8, 161.6, 157.7, 153.2, 130.4, 129.5, 128.2, 127.3, 124.9, 122.4, 120.7, 115.8, 111.1, 66.9, 59.9, 59.0, 55.7, 53.5, 52.5, 45.9, 38.0, 31.5, 29.8, 29.5, 27.7, 24.7.

ESI-MS (*m/z*): 633.3 [M + H]$^+$

4.3. Biological procedures

4.3.1. Protein preparation

M^{pro} SARS-CoV-2 and MERS-CoV were expressed in *E. coli* cells BL21 (DE3) and the expression pellets, after ultracentrifugation, were purified as described [35]. The fractions containing the M^{pro} SARS-2 were pooled and concentrated using Amicon Ultra 15 centrifugal filters, at 4000×*g*, at 4 °C, in a buffer exchange (20 mM Tris-HCl, 150 mM NaCl, 1 mM EDTA, 1 mM DTT, pH 7.8).

M^{pro} MERS-CoV protein was purified in two steps using a Ni-Sepharose column and by HiTrap Q HP column and the fractions containing the M^{pro} SARS-2 were pooled and concentrated using Amicon Ultra 15 centrifugal filters, at 4000×*g*, at 4 °C, in a buffer exchange (20 mM Tris-HCl, 150 mM NaCl, 1 mM EDTA, 1 mM DTT, pH 7.8). Protein purity was verified by SDS-PAGE analysis and the proteins were stored at −80 °C.

The M^{pro} SARS-CoV02 for crystallization was obtained from BL21 (DE) *E. coli* grown in YT medium using the pGEX vector provided from Hilgenfeld and coworkers [36]. Protein was purified following the protocol previously reported [20,37].

4.3.2. M^{pro} SARS-CoV-2 and MERS-CoV in vitro assays

The M^{pro} SARS-CoV-2 and MERS-CoV biochemical assays were performed in 386 wells plate in 20 μl of assay buffer containing diluted protein, 20 mM Tris (pH 7.3), 100 mM NaCl, 5 mM TCEP, 0.1% BSA and 1 mM EDTA [18,37]. The proteins were preincubated for 30 min at 37 °C with different concentrations of compounds. After the preincubation, the substrate DABCYL-KTSAVLQ↓SGFRKM-EDANS (Bachem) was added and the signal was monitored after 15 min and 30 min of incubation for M^{pro} SARS-CoV-2 and M^{pro} MERS, respectively. Generation of the fluorescent product was monitored (Ex 340 nm, Em 490 nm).

4.3.3. SARS-CoV-2 replication assay

Was performed as previously described [38]. Briefly, Vero E6-GFP (Janssen Pharmaceutical) were maintained in Dulbecco's modified Eagle's medium (DMEM; Gibco) supplemented with 10% v/v fetal beef serum (FBS; Gibco), 0.075% Sodium Bicarbonate (7.5% solution, Gibco) and 1x Pen-strep (Euroclone) and kept under 5% CO_2 on 37 °C. SARS-CoV-2 strain BetaCov/Belgium/GHB-03021/2020 was provided by KU Leuven. All virus-related work was carried out in certified, high-containment biosafety level-3 facilities at the University of Cagliari. Cells were seeded at 10000 cells/well in 96-well black cell-treated plates (PerkinElmer). The following day, cells were incubated with the control compounds at different concentrations and the virus at MOI 0.01. GC376 compound [35] was used as positive control, in presence of 2 μM p-gp inhibitor CP-100356 [39]. 72 h post infection the media was removed and total well GFP fluorescence was measured with a Victor 3 with 485/535 nm excitation wavelength. The inhibition of viral replication was calculated as percentage of viral induced cytopathic effect on infected untreated controls, minus blancs (empty wells). EC_{50} value was calculated with Prism 9. Version 9.1.2 via non-linear regression. The experiments represent average and standard deviation of at least two independent experiments in triplicate.

4.3.4. Evaluation of cytotoxicity

Vero E6-GFP cells were seeded at 10000 cells/well in 96-well black cell-treated plates, the following day, cells were incubated with the compounds for 72 h. The media was removed and total well GFP fluorescence was measured with a Victor 3 with 485/535 nm excitation wavelength. Cytotoxicity was calculated as a percentage of fluorescence of untreated controls, minus blancs (empty wells). CC_{50} value was calculated with Prism 9. Version 9.1.2 (225) via non-linear regression. The experiments represent average and standard deviation of at least two independent experiments in triplicate.

4.3.5. Protein crystallization and structure determination

Co-crystals of M^{pro} in complex with **9a** and **9e** were obtained by seeding techniques as previously described [37]. Briefly, each compound at a final concentration of 5 mM was preincubated for 1 h at RT with 5 mg/mL 3CLpro in 20 mM Tris-HCl, 150 mM NaCl, 1 mM EDTA, pH 7.8, 1 mM DTT. Crystallization trials were set up by seeding in sitting drops using the Morpheus® kit (Molecular Dimensions) with a Mosquito robot (STPlabtech Ltd., Melbourne Hertfordshire, UK). Crystals were flash frozen in liquid nitrogen after a few days of growth.

For compound **9a**, the best diffracting crystals grew in condition D9: 0.12 M 1,6-Hexanediol, 0.12 M 1-Butanol, 0.12 M 1,2-Propanediol, 0.12 M 2-Propanol, 0.12 M 1,4-Butanediol, 0.12 M 1,3-Propanediol, 0.1 M Tris/bicine pH 8.5, 20% v/v PEG 500 MME, 10% w/v PEG 20000. For compound **9e**, the best diffracting crystals grew in condition C5: 0.09 M Sodium nitrate, 0.09 Sodium phosphate dibasic, 0.09 M Ammonium sulfate, 0.1 M Hepes/MOPS pH 7.5, 20% v/v PEG 500 MME, 10% w/v PEG 20000. Diffraction data were collected at 100 K, at the XDR2 beamline of the Elettra synchrotron in Trieste using a 1.000 Å wavelength. The collected dataset was processed with XDS [40], and Aimless from the CCP4 suite [41]. The structure was solved by molecular replacement with Phaser [42] using as a search model 7BB2 (PDB ID). The initial model was refined alternating cycles of manual model building in COOT [43], and automatic refinement using Phenix (version 1.19.2–4085) [44]. Data collection and refinement statistics are reported in Table S1. Figures were prepared using Pymol [The PyMOL

Molecular Graphics System, Version 2.1 Schrödinger, LLC., New York, NY, USA].

Authors contributions

S.P.: conceptualization, methodology, investigation, project administration, writing – original draft, writing – review and editing; C.C.: computational studies, investigation, data curation; F.E.: formal analysis, investigation, data curation; R.C.; investigation, writing – original draft; A.C.; formal analysis, investigation, data curation; E.C.: formal analysis, investigation; M.K. formal analysis, investigation; P.G.: formal analysis, investigation, validation; A.Z.; supervision, validation; M.B.: supervision, review and editing; P.S.; formal analysis, validation, data curation, supervision, writing –review and editing; E.T.: resources, supervision; V.S.: conceptualization, funding acquisition, project administration, supervision, resources, writing –review and editing.

Declaration of competing interest

The authors declare that they have no known competing financial interests or personal relationships that could have appeared to influence the work reported in this paper.

Data availability

Data will be made available on request.

Acknowledgements

S.P. acknowledges MUR (Ministero dell'Università e della Ricerca), PON R&I 2014-2020- Asse IV "Istruzione e Ricerca per il recupero-REACT-EU", Azione IV.6 "Contratti di Ricerca su tematiche Green".

R.C. thanks MIUR-Ministero dell'Istruzione, dell'Università e della Ricerca (Italian Ministry of Education, University and Research), PON R&I 2014-2020- AIM (Attraction and International Mobility), project AIM1873131 Num. Attività 2 Linea 2.1.

C.C. thanks MUR (Ministero dell'Università e della Ricerca), PON R&I 2014-2020-Asse IV "Istruzione e Ricerca per il recupero-REACT-EU" Azione IV.4- Contratti di Ricerca su tematiche dell'innovazione.

Authors thank "EXaSCale smArt pLatform Against paThogEns for Corona Virus-Exscalate4CoV" founded by the EU's H2020-SC1-PHE-CORONAVIRUS 2020 call, grant no. 101003551.

Janssen Pharmaceutical for providing the African green monkey kidney cell line was engineered to constitutively express GFP (Vero E6-GFP) and Pieter Leyssen laboratory of KU Leuven for providing the SARS-CoV-2 strain BetaCov/Belgium/GHB-03021/2020, and Nicola Demitri from XRD2 beamline of Elettra Sincrotrone Trieste (Italy) for support in crystallographic data collection and refinement.

Appendix A. Supplementary data

Supplementary data to this article can be found online at https://doi.org/10.1016/j.ejmech.2022.114853.

Abbreviations

CoV	coronavirus
COVID-19	coronavirus disease 19
DMSO	dimethyl sulfoxide;
M^{pro}	SARS-CoV-2 main protease
DCM	dichloromethane
GSH	glutathione
ESI/MS	electrospray ionization mass spectrometry
MERS-CoV	Middle East respiratory syndrome
MDS	molecular dynamics simulation
NMR	nuclear magnetic resonance
PDB	Protein Data Bank
RNA	ribonucleic acid
SARS	severe acute respiratory syndrome
TLC	thin layer chromatography
IC_{50}	half maximal inhibitory concentrations
EC_{50}	half maximal effective concentration
CC_{50}	50% cytotoxic concentration
TCEP	tris(2-carboxyethyl)phosphine;
CMV	cytomegalovirus

References

[1] P. Zhou, X.-L. Yang, X.-G. Wang, B. Hu, L. Zhang, W. Zhang, H.-R. Si, Y. Yan Zhu, B. Li, C.-L. Chao-Lin Huang, H.-D. Chen, J. Chen, Y. Yun Luo, H. Hua Guo, R.-D. Jiang, M.-Q. Liu, Y. Ying Chen, X.-R. Shen, X. Wang, X.-S. Zheng, K. Zhao, Q.-J. Chen, F. Deng, L.-L. Liu, B. Yan, F.-X. Zhan, Y.-Y. Wang, G.-F. Xiao, Z.-L. Shi, A pneumonia outbreak associated with a new coronavirus of probable bat origin, Nature 579 (2020) 270–273.

[2] F. Wu, S. Zhao, B. Yu, Y.-M. Chen, W. Wang, Z.-G. Song, Y. Hu, Z.-W. Tao, J.-H. Tian, Y.-Y. Pei, M.-L. Yuan, Y.-L. Zhang, F.-H. Dai, Y. Liu, Q.-M. Wang, J.-J. Jiao-Jiao Zheng, L. Xu, E.C. Holmes, Y.-Z. Zhang, A new coronavirus associated with human respiratory disease in China, Nature 579 (2020) 265–269.

[3] Y. Chen, Q. Liu, D. Guo, Emerging coronaviruses: genome structure, replication, and pathogenesis, J. Med. Virol. 92 (2020) 418–423.

[4] R. Hilgenfeld, From SARS to MERS: crystallographic studies on coronaviral proteases enable antiviral drug design, FEBS J. 281 (2014) 4085–4096.

[5] K. Anand, J. Ziebuhr, P. Wadhwani, J.R. Mesters, R. Hilgenfeld, Coronavirus main proteinase (3CLpro) structure: basis for design of anti-SARS drugs, Science 300 (2003) 1763–1767.

[6] A. Wu, Y. Peng, B. Huang, X. Ding, X. Wang, P. Niu, J. Meng, Z. Zhu, Z. Zhang, J. Wang, J. Sheng, L. Quan, Z. Xia, W. Tan, G. Cheng, T. Jiang, Genome composition and divergence of the novel coronavirus (2019-nCoV) originating in China, Cell Host Microbe 27 (2020) 325–328.

[7] A.A.T. Naqvi, K. Fatima, T. Mohammad, U. Fatima, I.K. Singh, A. Singh, S.M. Atif, G. Hariprasad, G.M. Hasan, I. Md Hassan, Insights into SARS-CoV-2 genome, structure, evolution, pathogenesis and therapies: structural genomics approach, Biochim. Biophys. Acta, Mol. Basis Dis. 1866 (2020), 165878.

[8] a) R. Cannalire, C. Cerchia, A.R. Beccari, F.S. Di Leva, V. Summa, Targeting SARS-CoV-2 proteases and polymerase for COVID-19 treatment: state of the art and future opportunities, J. Med. Chem. 65 (2022) 2716–2746;
b) R. Cannalire, I. Irina Stefanelli, C. Cerchia, A.R. Beccari, S. Pelliccia, V. Summa, SARS-CoV-2 entry inhibitors: small molecules and peptides targeting virus or host cells, Int. J. Mol. Sci. 21 (2020) 5707.

[9] K. Fan, P. Wei, Q. Feng, S. Chen, C. Huang, L. Ma, B. Lai, J. Pei, Y. Liu, J. Chen, L. Lai, Biosynthesis, purification, and substrate specificity of severe acute respiratory syndrome coronavirus 3C-like proteinase, J. Biol. Chem. 279 (2004) 1637–1642.

[10] J. Shi, Z. Wei, J. Song, Dissection study on the severe acute respiratory syndrome 3C-like protease reveals the critical role of the extra domain in dimerization of the enzyme. Defining the extra domain as a new target for design of highly specific protease inhibitors, J. Biol. Chem. 279 (2004) 24765–24773.

[11] Z. Jin, X. Du, Y. Xu, Y. Deng, M. Liu, Y. Zhao, B. Zhang, X. Li, L. Zhang, C. Peng, Y. Duan, J. Yu, L. Wang, K. Yang, F. Liu, R. Jiang, X. Yang, T. You, X. Liu, X. Yang, F. Bai, H. Liu, X. Liu, L.W. Guddat, W. Xu, G. Xiao, C. Qin, Z. Shi, H. Hualiang Jiang, Z. Zihe Rao, H. Yang, Structure of Mpro from SARS-CoV-2 and discovery of its inhibitors, Nature 582 (2020) 289–293.

[12] L. Zhang, D. Lin, X. Sun, U. Curth, C. Drosten, L. Sauerhering, S. Becker, K. Rox, R. Hilgenfeld, Crystal structure of SARS-CoV-2 main protease provides a basis for design of improved a-ketoamide inhibitors, Science 368 (2020) 409–412.

[13] W. Dai, B. Zhang, X.-M. Jiang, H. Su, J. Li, Y. Zhao, X. Xie, Z. Jin, J. Peng, F. Liu, C. Li, Y. Li, F. Bai, H. Wang, X. Cheng, X. Cen, S. Hu, X. Yang, J. Wang, X. Liu, G. Xiao, H. Jiang, Z. Rao, L.-K. Lei-Ke Zhang, Y. Xu, H. Yang, H. Liu, Structure-based design of antiviral drug candidates targeting the SARS-CoV-2 main protease, Science 368 (2020) 1331–1335.

[14] D.R. Owen, C.M.N. Allerton, A.S. Anderson, L. Aschenbrenner, M. Avery, S. Berritt, B. Boras, R.D. Cardin, A. Carlo, K.J. Coffman, A. Dantonio, L. Di, H. Eng, R. Ferre, K.S. Gajiwala, S.A. Gibson, S.E. Greasley, B.L. Hurst, E.P. Kadar, A.S. Kalgutkar, J. C. Lee, J. Lee, W. Liu, S.W. Mason, S. Noell, J.J. Novak, R.S. Obach, K. Ogilvie, N. C. Patel, M. Pettersson, D.K. Rai, M.R. Reese, M.F. Sammons, J.G. Sathish, R.S. P. Singh, C.M. Steppan, A.E. Stewart, J.B. Tuttle, L. Updyke, P.R. Verhoest, L. Wei, Q. Yang, Y. Zhu, An oral SARS-CoV-2 Mpro inhibitor clinical candidate for the treatment of COVID-19, Science 374 (2021) 1586–1593.

[15] R. Oerlemans, A.J. Ruiz-Moreno, Y. Cong, N. Dinesh Kumar, M.A. Velasco-Velazquez, C.G. Neochoritis, J. Smith, F. Reggiori, M.R. Groves, A. Dömling, Repurposing the HCV NS3–4A protease drug boceprevir as COVID-19 therapeutics, RSC Med. Chem. 12 (2021) 370–379.

[16] Z. Xia, M. Sacco, Y. Hu, C. Ma, X. Meng, F. Zhang, T. Szeto, Y. Xiang, Y. Chen, J. Wang, Rational design of hybrid SARS-CoV-2 main protease inhibitors guided by the superimposed cocrystal structures with the peptidomimetic inhibitors GC-376, Telaprevir, and boceprevir, ACS Pharmacol. Transl. Sci. 4 (2021) 1408–1421.

[17] J. Qiao, Y.-S. Li, R. Zeng, F.-L. Liu, R.-H. Luo, C. Huang, Y.-F. Wang, J. Zhang, B. Quan, C. Shen, X. Mao, X. Liu, W. Sun, W. Yang, X. Ni, K. Wang, L. Xu, Z.-

L. Duan, Q.-C. Zou, H.-L. Hai-Lin Zhang, W. Qu, Y.-H.-P. Long, M.-H. Li, R.-C. Yang, X. Liu, J. You, Y. Zhou, R. Yao, W.-P. Li, J.-M. Liu, P. Chen, Y. Liu, G.-F. Lin, X. Yang, J. Zou, L. Li, Y. Hu, G.-W. Lu, W.-M. Li, Y.-Q. Wei, Y.-T. Zheng, J. Lei, S. Yang, SARS-CoV-2 Mpro inhibitors with antiviral activity in a transgenic mouse model, Science 371 (2021) 1374–1378.

[18] B. Boras, R.M. Jones, B.J. Banson, D. Arenson, L. Aschenbrenner, M.A. Bakowski, N. Beutler, J. Binder, E. Chen, H. Eng, H. Hammond, J. Hammond, R.E. Haupt, R. Hoffman, E.P. Kadar, R. Kania, E. Kimoto, M.G. Kirkpatrick, L. Lanyon, E. K. Lendy, J.R. Lillis, J. Logue, S.A. Luthra, C. Ma, S.W. Mason, M.E. McGrath, S. Noell, R.S. Scott Obach, M.N. O' Brien, R. O'Connor, K. Ogilvie, D. Owen, M. Pettersson, M.R. Reese, T.F. Rogers, R. Rosales, M.I. Rossulek, J.G. Sathish, N. Shirai, C. Steppan, M. Ticehurst, L.W. Updyke, S. Weston, Y. Zhu, K.M. White, A. García-Sastre, J. Wang, A.K. Chatterjee, A.D. Mesecar, M.B. Frieman, A. S. Anderson, C. Allerton, Preclinical characterization of an intravenous coronavirus 3CL protease inhibitor for the potential treatment of COVID19, Nat. Commun. 12 (2021) 6055.

[19] M. Robello, E. Barresi, E. Baglini, S. Salerno, S. Taliani, F. Da Settimo, The alpha keto amide moiety as a privileged motif in medicinal chemistry: current insights and emerging opportunities, J. Med. Chem. 64 (2021) 3508–3545.

[20] L. Zhang, D. Lin, Y. Kusov, Y. Nian, Q. Ma, J. Wang, A. Von Brunn, P. Leyssen, K. Lanko, J. Neyts, A. De Wilde, E.J. Snijder, H. Liu, R. Hilgenfeld, α-Ketoamides as broad-spectrum inhibitors of coronavirus and enterovirus replication: structure-based design, synthesis, and activity assessment, J. Med. Chem. 63 (2020) 4562–4578.

[21] L. Banfi, G. Guanti, R. Riva, Passerini multicomponent reaction of protected a-aminoaldehydes as a tool for combinatorial synthesis of enzyme inhibitors, Chem. Commun. 11 (2000) 985–986.

[22] L. Banfi, A. Basso, G. Guanti, R. Riva, Passerini reaction – amine Deprotection – acyl Migration (PADAM): a convenient strategy for the solid-phase preparation of peptidomimetic compounds, Mol. Divers. 6 (2003) 227–235.

[23] C. De Risi, G.P. Pollini, V. Zanirato, Recent developments in general methodologies for the synthesis of α-ketoamides, Chem. Rev. 116 (2016) 3241–3305.

[24] G. Koopmanschap, E. Ruijter, R.V.A. Orru, Isocyanide-based multicomponent reactions towards cyclic constrained peptidomimetics, Beilstein J. Org. Chem. 10 (2014) 544–598.

[25] A. Thakur, G. Sharma, V.N. Badavath, V. Jayaprakash, K.M. Merz Jr., G. Blum, O. Acevedo, Primer for designing main protease (Mpro) inhibitors of SARS-CoV-2, J. Phys. Chem. Lett. 13 (2022), 5776−578613.

[26] K. Zhu, K.W. Borrelli, J.R. Greenwood, T. Day, R. Abel, R.S. Farid, E. Harder, Docking covalent inhibitors: a parameter free approach to pose prediction and scoring, J. Chem. Inf. Model. 54 (2014) 1932–1940.

[27] Michael Dominic Sacco, et al., Structure and inhibition of the SARS-CoV-2 main protease reveal strategy for developing dual inhibitors against Mpro and cathepsin L, Sci. Adv. 6 (50) (2020), eabe0751.

[28] S.E. Greasley, S. Noell, O. Plotnikova, R. Ferre, W. Liu, B. Bolanos, K. Fennell, J. Nicki, T. Craig, Y. Zhu, A.E. Stewart, C.M. Steppan, Structural basis for the in vitro efficacy of nirmatrelvir against SARS-CoV-2 variants, J. Biol. Chem. 298 (2022), 101972.

[29] A. Thakur, G. Sharma, V.N. Badavath, V. Jayaprakash, K.M. Merz Jr., G. Blum, O. Acevedo, Primer for designing main protease (Mpro) inhibitors of SARS-CoV-2, J. Phys. Chem. Lett. 13 (2022) 5776–5786.

[30] L. Fu, F. Ye, Y. Feng, F. Yu, Q. Wang, Y. Wu, C. Zhao, H. Sun, B. Huang, P. Niu, H. Song, Y. Shi, X. Li, W. Tan, J. Qi, G.F. Gao, Both Boceprevir and GC376 efficaciously inhibit SARS-CoV-2 by targeting its main protease, Nat. Commun. 11 (2020) 4417.

[31] S. Tomar, M.L. Johnston, S.E.S. John, H.L. Osswald, P.R. Nyalapatla, L.N. Paul, A. K. Ghosh, M.R. Denison, A.D. Mesecar, Ligand-induced dimerization of Middle East Respiratory Syndrome (MERS) Coronavirus nsp5 protease (3CLpro): implications for nsp5 regulation and the development of antivirals, J. Biol. Chem. 290 (2015) 19403–19422.

[32] L. Ivanova, K. Rausalu, M. Ošeka, D.G. Kananovich, Z. Žusinaite, J. Tammiku-Taul, M. Lopp, A. Merits, M. Karelson, Novel analogues of the chikungunya virus protease inhibitor: molecular design, synthesis, and biological evaluation, ACS Omega 6 (16) (2021) 10884–10896.

[33] P. Patil, M. Ahmadian-Moghaddam, A. Dömling, Isocyanyde 2.0, Green Chem. 22 (2020) 6902–6911.

[34] Z.-X. Wang, J.-L. Chen, C. Qiao, Praziquantel derivatives with antischistosomal activity: aromatic ring modification, Chem. Biol. Drug Des. 82 (2013) 216–225.

[35] M. Kuzikov, E. Costanzi, J. Reinshagen, F. Esposito, L. Vangeel, M. Wolf, B. Ellinger, C. Claussen, G. Geisslinger, A. Corona, D. Iaconis, C. Talarico, C. Manelfi, R. Cannalire, G. Rossetti, J. Gossen, S. Albani, F. Musiani, K. Herzog, Y. Ye, B. Giabbai, N. Demitri, D. Jochmans, S. De Jonghe, J. Rymenants, V. Summa, E. Tramontano, A.R. Beccari, P. Leyssen, P. Storici, J. Neyts, P. Gribbon, A. Zaliani, Identification of inhibitors of SARS-CoV-2 3CL-pro enzymatic activity using a small molecule in vitro repurposing screen, ACS Pharmacol. Transl. Sci. 4 (2021) 1096–1110.

[36] D.Z. Lin, W.K. Qian, R. Hilgenfeld, H.L. Jiang, K.X. Chen, H. Liu, Improved synthesis of rupintrivir, Sci. China Chem. 55 (2012) 1101–1107.

[37] E. Costanzi, M. Kuzikov, F. Esposito, S. Albani, N. Demitri, B. Giabbai, M. Camasta, E. Tramontano, G. Rossetti, A. Zaliani, et al., Structural and biochemical analysis of the dual inhibition of MG-132 against SARS-CoV-2 main protease (Mpro/3CLpro) and human cathepsin-L, Int. J. Mol. Sci. 22 (2021), 11779.

[38] A. Corona, K. Wycisk, C. Talarico, C. Manelfi, J. Milia, R. Cannalire, F. Esposito, P. Gribbon, A. Zaliani, D. Iaconis, A. Beccari, V. Summa, Natural compounds inhibit SARS-CoV-2 nsp13 unwinding and ATPase enzyme activities, ACS Pharmacol. Transl. Sci 5 (2022) 226–239.

[39] Y. Hu, C. Ma, T. Szeto, B. Hurst, B. Tarbet, J. Wang, Boceprevir, calpain inhibitors II and XII, and GC-376 have broad-spectrum antiviral activity against coronaviruses, ACS Infect. Dis. 7 (2021) 586–597.

[40] W. Kabsch, XDS. Acta Cryst 66 (2010) 125–132.

[41] M.D. Winn, C.C. Ballard, K.D. Cowtan, E.J. Dodson, P. Emsley, P.R. Evans, R. M. Keegan, E.B. Krissinel, A.G.W. Leslie, A. McCoy, S.J. McNicholas, G. N. Murshudov, N.S. Pannu, E.A. Potterton, H.R. Powell, R.J. Read, A. Vagin, K. S. Wilson, Overview of the *CCP*4 suite and current developments, Acta Crystallogr. 67 (2011) 235–242.

[42] A.J. McCoy, R.W. Grosse-Kunstleve, P.D. Adams, M.D. Winn, L.C. Storoni, R. J. Read, Phaser crystallographic software, J. Appl. Crystallogr. 40 (2007) 658–674.

[43] P. Emsley, K. Cowtan, Coot: model-building tools for molecular graphics, Acta Crystallogr. 60 (2004) 2126–2132.

[44] D. Liebschner, P.V. Afonine, M.L. Baker, G. Bunkóczi, V.B. Chen, T.I. Croll, B. Hintze, L.-W. Hung, S. Jain, A.J. McCoy, N.W. Moriarty, R.D. Oeffner, B.K. Poon, M.G. Prisant, R.J. Read, J.S. Richardson, D.C. Richardson, M.D. Sammito, O. V. Sobolev, D.H. Stockwell, T.C. Terwilliger, A.G. Urzhumtsev, L.L. Videau, C. J. Williams, P.D. Adams, Macromolecular structure determination using X-rays, neutrons and electrons: recent developments in Phenix, Acta Crystallogr. 75 (2019) 861–877.